

Ground-based radar observations of Titan: 2000–2008

G.J. Black^{a,*}, D.B. Campbell^b, L.M. Carter^c

^a Department of Astronomy, University of Virginia, PO Box 400325, Charlottesville, VA 22904, United States

^b Department of Astronomy, Cornell University, 528 Space Sciences Bldg., Ithaca, NY 14853, United States

^c NASA Goddard Space Flight Center, Code 698, Greenbelt, MD 20771, United States

ARTICLE INFO

Article history:

Received 1 April 2010

Revised 16 October 2010

Accepted 29 October 2010

Available online 6 November 2010

Keywords:

Titan

Saturn, Satellites

Radar observations

ABSTRACT

We have observed Titan with the Arecibo Observatory's 12.6 cm wavelength radar system during the last eight oppositions of the Saturn system with sufficient sensitivity to characterize its scattering properties as a function of sub-Earth longitude. In a few sessions the Green Bank Telescope was used as the receiving instrument in a bistatic configuration to boost sub-radar track length and integration time. Radar echo spectra have been obtained for a total of 92 viewing geometries with sub-Earth locations scattered through all longitudes and at latitudes between 7.6°S and 26.3°S, close to the maximum southern excursion of the sub-Earth track. We find Titan to have globally average radar albedos at this wavelength of 0.161 in the opposite circular polarization sense as that transmitted (OC) and 0.074 in the same sense (SC), giving a polarization ratio SC/OC of 0.46. These values are intermediate between lower reflectivity rocky surfaces and higher reflectivity clean icy surfaces. The variations with longitude in general mirror the surface brightness variations seen through the infrared atmospheric windows. Xanadu Regio's radar reflectivity and polarization ratio are higher than the global averages, and suggest that its composition is relatively cleaner water ice or, possibly, some other material with low propagation loss at radio wavelengths. For all echo spectra most of the power is in a broad diffuse component but with a specular component whose strength and narrowness is highly variable as a function of surface location. For all data we fit a sum of the standard Hagfors scattering law describing the specular component and an empirical diffuse radar scattering model to extract bulk parameters of the surface. Many areas exhibit very narrow specular reflections implying terrain that are quite flat on centimeter to meter scales over spans of tens to perhaps hundreds of kilometers. The proportion of spectra showing these narrow specular echoes has fallen significantly over the observational time span, indicating either a latitudinal effect related to terrain differences or changing surface conditions over the past several years. A few radar tracks, especially those from the 2008 session, overlap some high resolution Cassini RADAR imagery swaths to allow a direct comparison with terrain.

© 2011 Elsevier Inc. All rights reserved.

1. Introduction

Titan has proved to be a surprisingly dynamic world and in many ways quite Earth-like. Observations of the high abundance of methane in its nitrogen atmosphere led to suspicion that there might be a surface–atmosphere methane cycle similar to Earth's water cycle (Owen, 1982; Atreya et al., 2006). New evidence, particularly from Cassini, demonstrates this is truer than was expected with observations providing evidence for wind processes (Radebaugh et al., 2008; Lorenz et al., 2006), continuing erosion (Lorenz et al., 2007; Barnes et al., 2007b; Elachi et al., 2006), clouds (Brown et al., 2002; Griffith et al., 1998), and even apparent liquid bodies (Stofan et al., 2007). Changes due to an active methane cycle (Turtle et al., 2009) and possible recent cryovolcanic activity (Lopes

et al., 2007; Wall et al., 2009) further strengthens the Earth-like parallels. As a result of these processes Titan is covered by a wide variety of landscapes from deserts to drainage systems to suspected volcanic areas.

Radar provides a unique view of planetary surfaces and the near sub-surface, probing at least several wavelengths deep into typical non-ice targets, but potentially much deeper into the low absorption layers of predominantly icy surfaces. Water ice by itself has extremely low radio-wavelength absorption (Thompson and Squyres, 1990; Warren, 1984), providing opportunities for higher order scattering phenomena within the near sub-surface. The strength, polarization, and angular scattering characteristics of reflected energy from a target contain information on the scattering mechanism and in turn the structure and composition of the layers from which those echoes originate. For Titan, radar fills an especially important role by providing a clear window through its atmosphere and haze layers which have made studies of its surface difficult at other wavelengths.

* Corresponding author.

E-mail address: gblack@virginia.edu (G.J. Black).

The first efforts to detect Titan with ground-based radar were made in 1989 (Muhleman et al., 1990) using the Goldstone 3.5 cm wavelength radar transmitter with reception of the echoes at the Very Large Array, imaging the echo power in the opposite (OC) and same (SC) circular senses relative to the transmitted polarization. That and subsequent experiments through 1992 (Muhleman et al., 1993) found Titan's reflectivity to be moderately high with an average of 0.22 in the OC polarization sense, but with large uncertainties. Improved observations in 1993 (Muhleman et al., 1995) gave a better estimate of Titan's global reflectivity at 3.5 cm wavelength to be 0.13 ± 0.02 in the OC polarization sense, with generally much weaker or undetected power in the SC polarization. Longitudinal variations were seen, with the leading hemisphere (longitudes $< 180^\circ\text{W}$) $\sim 50\%$ more reflective than the trailing hemisphere (longitudes $> 180^\circ\text{W}$), although some of the variations are difficult to reconcile with the relatively flat scattering law versus incidence angle that was also reported from that work. Nonetheless, these first radar observations ruled out the existence of a global ocean as had been suggested by some photochemical models (Lunine et al., 1983).

More recently, the Cassini RADAR instrument (Elachi et al., 2005) is providing very high resolution radar imagery of narrow swathes of the surface when in SAR mode (cf. Lunine et al.,

2008), as well as lower resolution data over wider areas when in scatterometry mode (cf. Wye et al., 2007). Both datasets but especially the SAR mode are excellent for imaging surface features and distinguishing terrain units, and have already yielded many surprising results.

Earth-based radar observations measure the scattering properties over an entire hemisphere but at a coarse resolution compared to the targeted observations made by the Cassini RADAR. The observations of Titan we report here were made at 12.6 cm wavelength which probe the scattering properties at surface scales six times larger than the 2.2 cm wavelength Cassini RADAR, and in addition we obtain dual circular polarization data in contrast to Cassini's single linear polarization. The analysis here particularly focuses on the normal incidence properties of the surface, for which the measurement of the specular (mirror-like) echo that results from single scattering off the surface can give estimates of the surface slopes over scales comparable to the wavelength, and assuming a homogeneous surface, the Fresnel reflectivity from which the surface dielectric constant can be obtained.

This paper begins by presenting the full Arecibo dataset and derived estimates of disk integrated reflectivity versus longitude. We fit standard Hagfors and diffuse scattering laws to this ground-based data to extract physical parameters describing the surface, and make a rough attempt at better isolation of those parameters versus longitude by rebinning a subset of the data to remove the frequency drift of any given longitude as our view of Titan rotates. Some interesting features of the dataset are then discussed, namely those containing strong and variable specular echoes, and data from periods when the sub-Earth track passed over Cassini SAR imagery swathes. One of those Cassini tracks (T8) included extensive areas of sand dunes (Lorenz et al., 2006) while several (T13, T41, T43, T44) passed over Xanadu Regio.

2. Observations

We have used the Arecibo Observatory's 12.6 cm wavelength (2.38 GHz) radar system to observe Titan near each opposition from 2000 through 2008. Due to the great distance to the Saturn system opposition observations are necessary to minimize the distance and thus maximize the echo strength.

The Arecibo Observatory's view of the sky is limited to zenith angles less than $\sim 20^\circ$, affording a maximum tracking time of $\sim 2\text{ h:}45\text{ m}$ for an object passing near the zenith. At opposition the light travel time from the Earth to the Saturn system and back is of order $2\text{ h:}15\text{ m}$, leaving at most only $\sim 30\text{ min}$ of time per day

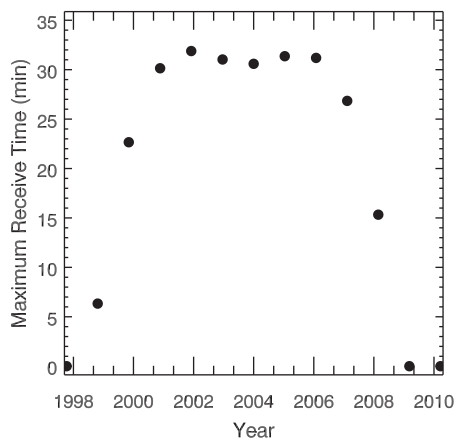


Fig. 1. Maximum daily time that was available to observe Titan using Arecibo as both the transmit and receive station (monostatic mode) is shown. The round trip light travel time to Saturn is at least $\sim 2\text{ h:}15\text{ m}$ and the maximum tracking time of Arecibo is $\sim 2\text{ h:}45\text{ m}$. There is one point for each opposition of the Saturn system, and the time drops to zero when its declination is below that observable from Arecibo.

Table 1
System parameters.

Session	2000	2001	2002	2004	2005	2006	2007	2008
First date	November 03	November 25	November 23	January 02	January 10	January 12	January 19	February 09
Last date	November 27	January 11 ^a	December 30	January 12	January 29	February 03	February 17	February 23
<Power> (kW)	909	889	889	718	775	439	679	701
<Distance> (AU)	8.16	8.10	8.06	8.06	8.09	8.14	8.23	8.31
Arecibo receive:								
# of days	8	17	9	8	8	10	12	9
Max Gain (K/Jy)	5.8	9.3	9.3	9.8	9.8	9.8	9.8	9.8
OC T_{sys} (K)	28.0	28.6	30.1	26.2	31.3	27.2	26.2	25.1
SC T_{sys} (K)	26.9	26.3	25.3	29.6	34.6	28.8	29.0	31.0
GBT receive:								
# of days		3 ^b	15 ^b					11
Gain (K/Jy)		1.9	1.9					1.9
OC T_{sys} (K)		30	30					29.9
SC T_{sys} (K)		30	30					33.9

^a 2002.

^b Gains and system temperatures estimated.

Table 2
Observation log.

Date (UTC)	RX ^a	Sub-radar point		τ_{int} (min)	RTT (s)	SNR		$\hat{\sigma}_{OC}$	$\hat{\sigma}_{SC}$	μ_C
		W. Lon.	Lat.			OC	SC			
2000 November 03	A	163.1	−23.6	24.0	8150.7	141	61	0.17	0.07	0.43
2000 November 04	A	185.7	−23.6	25.3	8145.6	119	44	0.13	0.05	0.37
2000 November 05	A	208.4	−23.6	24.7	8141.9	168	45	0.19	0.05	0.27
2000 November 06	A	231.0	−23.5	24.7	8139.6	118	59	0.14	0.06	0.44
2000 November 07	A	253.6	−23.5	28.7	8138.4	183	71	0.19	0.06	0.34
2000 November 08	A	276.2	−23.5	26.0	8137.7	135	45	0.16	0.05	0.31
2000 November 09	A	298.7	−23.5	28.7	8137.3	151	49	0.16	0.05	0.33
2000 November 27	A	345.6	−23.2	14.7	8133.9	103	60	0.16	0.10	0.64
2001 November 25	A	245.5	−25.6	24.0	8072.3	312	116	0.12	0.04	0.34
2001 November 26	A	268.1	−25.6	24.7	8072.8	294	148	0.11	0.05	0.46
2001 November 27	A	290.7	−25.6	21.3	8073.6	284	130	0.11	0.05	0.42
2001 November 28	A	313.3	−25.6	24.0	8074.2	291	152	0.11	0.05	0.48
2001 November 29	A	335.8	−25.6	20.0	8074.2	272	120	0.13	0.05	0.41
2001 November 30	A	358.4	−25.6	24.0	8073.5	369	160	0.14	0.06	0.40
2001 December 01	A	21.0	−25.6	24.7	8072.0	403	221	0.15	0.08	0.51
2001 December 02	A	43.6	−25.6	24.0	8069.8	400	209	0.15	0.07	0.48
2001 December 03	A	66.2	−25.6	23.3	8067.2	432	256	0.16	0.09	0.54
2001 December 06	A	134.0	−25.6	19.3	8060.6	394	214	0.17	0.09	0.50
2001 December 07	A	156.6	−25.6	24.7	8060.0	388	158	0.15	0.05	0.38
2001 December 08	A	179.2	−25.6	24.0	8060.7	301	139	0.11	0.05	0.43
2001 December 09	A	201.8	−25.6	23.3	8062.9	284	138	0.11	0.05	0.45
2001 December 10	A	224.5	−25.6	24.7	8066.5	304	131	0.11	0.05	0.40
2001 December 20	A	90.3	−25.5	21.3	8108.1	442	233	0.20	0.10	0.48
2001 December 21	A	113.0	−25.5	28.0	8110.7	451	235	0.18	0.09	0.48
2002 January 11	A	227.2	−25.5	27.3	8285.0	264	92	0.11	0.03	0.32
2002 November 23	A	145.2	−26.1	6.7	8121.6	156	12	0.14	0.01	0.07
2002 December 16	A	304.7	−26.2	30.0	8040.8	338	138	0.13	0.04	0.34
2002 December 22	A	80.3	−26.3	27.3	8040.4	526	292	0.21	0.10	0.47
2002 December 23	A	102.8	−26.3	30.0	8039.3	473	325	0.18	0.10	0.58
2002 December 24	A	125.5	−26.3	30.0	8038.7	450	293	0.16	0.09	0.55
2002 December 27	A	193.3	−26.3	29.3	8043.5	323	156	0.12	0.05	0.41
2002 December 28	A	215.9	−26.3	29.3	8048.0	317	153	0.12	0.05	0.41
2002 December 29	A	238.6	−26.3	30.0	8053.6	271	142	0.10	0.04	0.44
2002 December 30	A	261.1	−26.3	30.0	8060.2	288	149	0.10	0.05	0.44
2004 January 02	A	273.6	−25.2	29.3	8035.4	295	113	0.12	0.05	0.44
2004 January 03	A	296.2	−25.2	29.3	8038.9	322	150	0.11	0.06	0.52
2004 January 04	A	318.8	−25.2	24.7	8042.0	330	131	0.12	0.05	0.46
2004 January 05	A	341.4	−25.2	29.3	8044.6	447	158	0.15	0.06	0.41
2004 January 09	A	71.7	−25.3	26.7	8047.8	642	282	0.21	0.11	0.51
2004 January 10	A	94.3	−25.3	29.3	8047.9	689	290	0.22	0.10	0.46
2004 January 11	A	116.9	−25.4	24.7	8048.3	606	239	0.20	0.09	0.45
2004 January 12	A	139.5	−25.4	29.3	8049.5	610	243	0.19	0.08	0.45
2005 January 10	A	62.2	−22.4	26.7	8065.1	458	243	0.18	0.10	0.59
2005 January 11	A	84.7	−22.5	30.0	8061.4	599	315	0.21	0.12	0.59
2005 January 12	A	107.3	−22.5	29.3	8057.8	496	334	0.18	0.13	0.74
2005 January 13	A	129.9	−22.5	30.7	8054.9	493	248	0.18	0.10	0.56
2005 January 19	A	265.8	−22.7	12.7	8064.3	206	84	0.12	0.06	0.46
2005 January 21	A	310.8	−22.7	29.3	8073.7	378	168	0.14	0.07	0.49
2005 January 28	A	108.8	−22.9	26.7	8090.0	588	271	0.24	0.12	0.51
2005 January 29	A	131.4	−22.9	26.0	8092.2	578	226	0.24	0.10	0.43
2006 January 12	A	53.5	−18.1	29.3	8153.3	325	158	0.20	0.10	0.51
2006 January 13	A	76.1	−18.1	29.3	8145.9	340	169	0.22	0.11	0.52
2006 January 14	A	98.7	−18.1	29.3	8138.5	293	160	0.19	0.10	0.57
2006 January 15	A	121.4	−18.2	29.3	8131.6	318	147	0.20	0.09	0.48
2006 January 24	A	324.7	−18.4	30.0	8119.4	231	79	0.13	0.05	0.38
2006 January 25	A	347.2	−18.5	30.0	8119.5	215	105	0.13	0.07	0.53
2006 January 26	A	9.8	−18.5	30.0	8118.8	219	94	0.13	0.06	0.46
2006 January 27	A	32.4	−18.5	30.0	8117.3	315	141	0.18	0.09	0.48
2006 February 01	A	145.3	−18.7	29.3	8107.6	288	94	0.16	0.06	0.37
2006 February 03	A	190.5	−18.8	30.0	8109.9	196	70	0.12	0.04	0.38
2007 January 19	A	158.9	−12.9	23.3	8254.4	308	145	0.15	0.08	0.53
2007 January 20	A	181.5	−12.9	23.3	8247.2	277	144	0.13	0.08	0.58
2007 January 25	A	294.5	−13.1	12.7	8229.8	191	42	0.13	0.03	0.26
2007 January 28	A	2.2	−13.2	24.7	8220.2	306	135	0.15	0.07	0.49
2007 January 29	A	24.7	−13.2	24.7	8215.4	382	142	0.17	0.07	0.43
2007 January 30	A	47.3	−13.2	24.7	8209.9	450	197	0.20	0.10	0.47
2007 February 01	A	92.4	−13.3	25.3	8197.7	449	228	0.20	0.11	0.57
2007 February 02	A	115.0	−13.4	25.3	8192.0	461	218	0.20	0.11	0.53
2007 February 03	A	137.6	−13.4	25.3	8187.0	401	205	0.17	0.10	0.57
2007 February 04	A	160.2	−13.4	25.3	8183.2	223	111	0.18	0.07	0.42
2007 February 05	A	182.8	−13.5	25.3	8181.0	354	170	0.16	0.09	0.54
2007 February 17	A	93.8	−13.9	26.0	8190.6	637	290	0.22	0.11	0.51
2008 February 09	A	222.1	−7.6	11.3	8304.4	118	17	0.07	0.01	0.16

Table 2 (continued)

Date (UTC)	RX ^a	Sub-radar point		τ_{int} (min)	RTT (s)	SNR		$\hat{\sigma}_{OC}$	$\hat{\sigma}_{SC}$	μ_c
		W. Lon.	Lat.			OC	SC			
2008 February 09	G			138.0						
2008 February 10	A	244.7	−7.6	11.3	8302.6	193	42	0.11	0.03	0.24
2008 February 10	G			114.0						
2008 February 11	A	267.3	−7.7	12.0	8301.5	206	111	0.12	0.07	0.59
2008 February 11	G			133.3						
2008 February 12	A	289.9	−7.7	12.0	8300.7	228	57	0.12	0.03	0.27
2008 February 12	G			138.0						
2008 February 13	A	312.5	−7.7	12.0	8299.7	270	77	0.15	0.05	0.31
2008 February 13	G			136.7						
2008 February 18	G	65.5	−7.9	105.3	8284.2	168	36	0.29	0.06	0.19
2008 February 19	A	87.9	−8.0	11.3	8279.5	292	139	0.20	0.10	0.52
2008 February 19	G			135.3						
2008 February 20	G	111.0	−8.0	88.7	8274.8	177	96	0.27	0.13	0.49
2008 February 21	A	133.1	−8.1	12.7	8271.1	184	72	0.11	0.05	0.44
2008 February 21	G			128.7						
2008 February 22	A	155.6	−8.1	12.7	8268.5	239	99	0.15	0.07	0.48
2008 February 22	G			58.0						
2008 February 23	A	178.2	−8.1	13.3	8267.3	198	90	0.12	0.06	0.53
2008 February 23	G			137.3						

Average statistical uncertainties are 3.5%, 4.7%, and 6.0% on $\hat{\sigma}_{OC}$, $\hat{\sigma}_{SC}$, and μ_c respectively.

^a Receiver: A = Arecibo, G = GBT. If both were used then only the summed result is listed.

Table 3

Pre-2008 GBT observation log.

Date (UTC)	Sub-radar point		τ_{int} (min)	RTT (s)	SNR	
	W. Lon.	Lat.			OC	SC
2001 December 06	134.8	−25.6	87.3	8060.6	113	54
2001 December 07	157.8	−25.6	79.3	8060.0	3	−23
2001 December 21	113.8	−25.5	134.0	8110.7	278	100
2002 November 20	78.2	−26.1	103.3	8152.3	248	124
2002 November 21	100.8	−26.1	102.0	8141.5	261	122
2002 November 22	123.5	−26.1	78.0	8130.9	198	103
2002 December 14	260.6	−26.2	98.7	8036.8	183	82
2002 December 16	305.5	−26.2	56.0	8040.8	148	81
2002 December 17	328.3	−26.2	98.7	8042.4	214	92
2002 December 19	13.5	−26.2	68.0	8043.4	178	35
2002 December 20	36.1	−26.2	96.0	8042.8	224	97
2002 December 21	58.7	−26.2	100.0	8041.7	283	151
2002 December 23	104.1	−26.3	76.0	8039.2	255	127
2002 December 24	126.3	−26.3	132.7	8038.7	308	203
2002 December 27	194.1	−26.3	111.3	8043.5	224	58
2002 December 28	216.7	−26.3	132.7	8048.0	224	86
2002 December 30	262.0	−26.3	134.0	8060.2	192	88
2002 December 31	285.3	−26.3	105.3	8067.5	174	90

to also receive the echo at Arecibo, known as a monostatic observation. Depending on the declination the tracking time may be less and is shown as a function of year in Fig. 1. This pattern will not repeat until the observing time is non-zero again in 2028.

For some runs the echo was also received with the 100 m Green Bank Telescope (GBT), in what is known as a bistatic observation, allowing reception of the full ~2.5 h Arecibo transmit or possibly ~2 h reception at the GBT together with the shorter Arecibo reception. If both systems received on a given day, combining their data would then boost the total signal-to-noise ratio, although generally Arecibo still had the greater sensitivity by at least a factor of 2 as its larger collecting area compensated for its shorter observing time. The sensitivities of the two systems were more comparable on days with very short Arecibo tracks, such as during the 2008 session or at other times when equipment problems reduced the receiving time. Besides sensitivity, a key motivation for acquiring the longer GBT tracks was that they sample a longer track of sub-radar location on Titan. At Titan's rotation rate a 30 min Arecibo track covers 0.5° of rotation (~20 km) while a 2.5 h GBT track covers 2.4° (~100 km).

Table 1 lists the average observing parameters for each session. At Arecibo the system temperatures were regularly measured by injecting a noise diode of known temperature into the system path. The telescope gain was taken from observations of standard flux calibrators (cf. Heiles et al. (2000), <http://www.naic.edu/~astro/RXstatus/>). A similar process was performed to calibrate the GBT data in the 2008 session, and the resulting estimates of Titan's reflectivity match those made by Arecibo on the same dates to within the statistical uncertainties. In earlier years less attention was paid to the calibration of the GBT data as the primary intent was to obtain a longer track rather than boost the total SNR. Those years' GBT data do not have sufficiently good calibration to be confidently used to measure the absolute reflectivity, but instead they are useful for sensing relative changes in the amplitude or shape of the echo spectrum during the tracks.

As an additional calibration, a few observations of the icy Galilean satellites Ganymede and Callisto were observed during the 2000 and 2002 sessions. In subsequent years the Jupiter system was at declinations not observable from Arecibo. The icy Galilean satellites are strong targets and have a history of observations with the Arecibo system since 1975 (Campbell et al., 1977) with very consistent estimates of their radar properties. Our observations of Ganymede and Callisto gave estimates of their radar reflectivities matching those from the extensive observations of them reported by Ostro et al. (1992) to within the statistical uncertainties.

Here we will use only the uncertainties based on the noise statistics. These statistical uncertainties will scale roughly as $T_{sys}/(PG_tG_r\sqrt{\tau})$ for system temperature T_{sys} , transmitted power P , integration time τ , and transmitting and receiving telescope gains G_t and G_r . Systematic errors could be larger and at worst are estimated to be as much as 25%, reflecting 10% errors each in the power, temperature, and gains. However, assuming a reasonable system stability, any systematic error should be constant at least during an observing session. In addition, the consistency of the year-to-year estimates of Titan's radar properties here as well as the reproducibility of the icy Galilean satellite results over several decades (Campbell et al., 1977, 1978; Ostro et al., 1992) with the Arecibo system, including our own measurements, argue that the system has been well characterized by the calibration efforts. Thus we expect any systematic error to be at least constant over this decade-long observing period and likely on the order of, or less

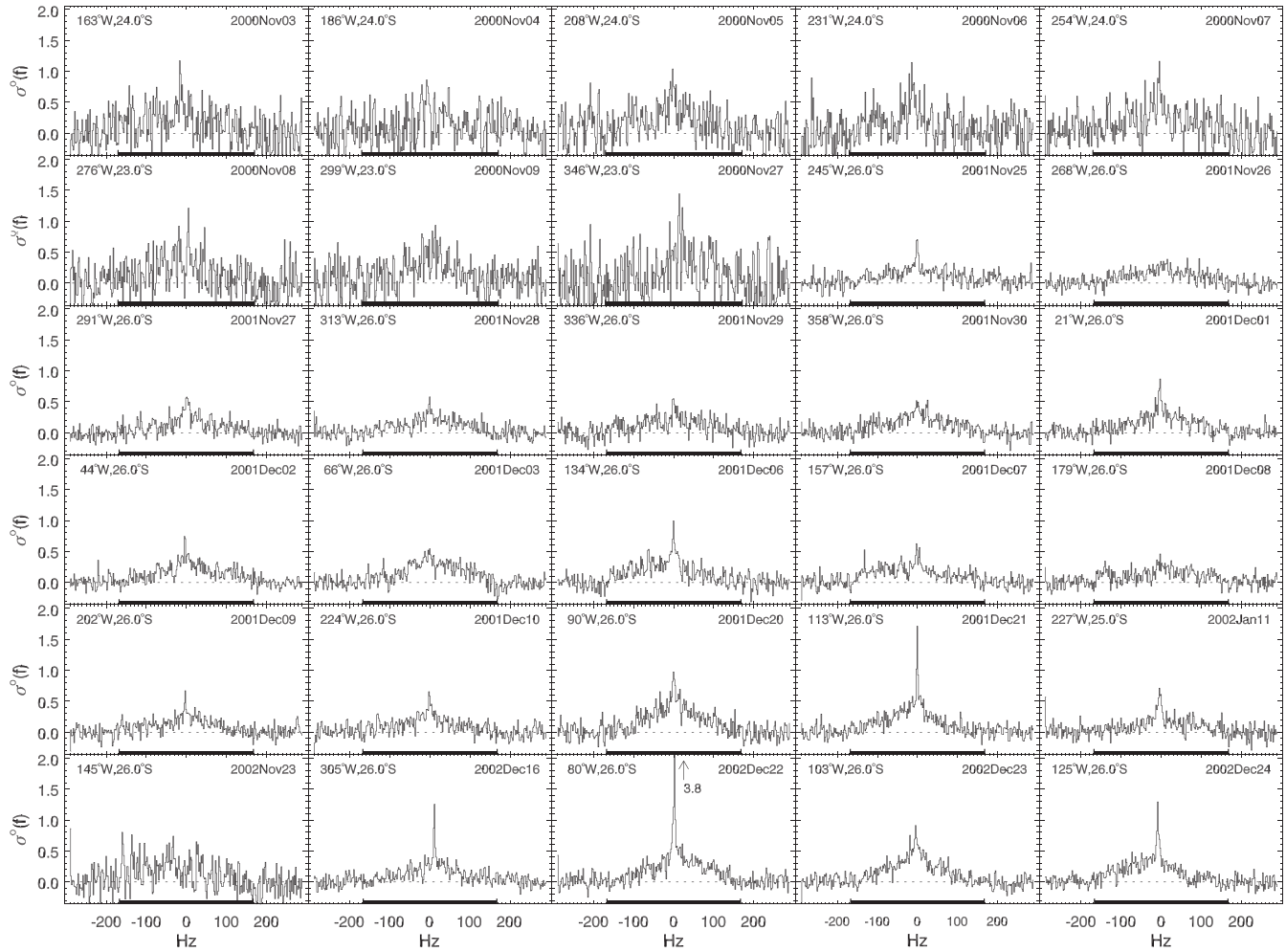


Fig. 2. Each panel shows a Titan echo spectrum obtained at Arecibo in the OC polarization channel on a single day. If both GBT and Arecibo data were obtained on the same date in 2008 then their combined spectrum is shown (see Table 2). The observation date and location of the sub-radar point on Titan are indicated on each. The sub-radar location corresponds to the center of the echo spectrum, and the full spectrum contains contributions from the entire Earth-facing hemisphere. The width of the echo is indicated by the solid bar on the abscissa and varies slightly depending on the latitude of the sub-radar point. The frequency resolution is 2 Hz, which at the sub-radar location corresponds to ~ 28 km along the surface and incidence angles $\leq 0.3^\circ$. The vertical scale is in units of specific radar cross section per bin. The peaks of some of the highest central spikes are indicated when they extend outside the plot range.

than, the statistical uncertainties. Finally we note that the circular polarization ratio, which is diagnostic of the scattering mechanism and is simply defined to be the ratio of the radar cross sections in the two polarizations, should be relatively unaffected by systematic errors.

On each date a monochromatic circularly polarized signal was transmitted and the echo received in both the same circular (SC) and opposite circular (OC) polarizations relative to the transmission. As Titan rotates the projected velocities of different surface areas induce Doppler shifts on the reflected signal, spreading the echo over a bandwidth in Hz given by

$$B = \frac{4\pi D}{\lambda P} \cos \delta, \quad (1)$$

where D and P are Titan's diameter and rotation period respectively, taken here to be 5150 km (Seidelmann et al., 2006) and 15.95 days (synchronous), and δ is the Titan latitude of the sub-radar point. At Arecibo's radar wavelength of 12.6 cm the maximum bandwidth is 372 Hz when Titan is observed directly over its equator. In practice the transmitted signal was also continuously frequency drifted to compensate for the relative motion between the observatory and the center-of-mass of Titan so that on reception the echo would

be centered at a constant frequency. The echo spectrum that results can be envisioned as the scan of a slit across the target's disk. The central bin of the spectrum crosses over the sub-radar point where the incidence angle is normal to the line-of-sight, and successively higher or lower frequencies move toward opposite limbs which will define the maximum frequencies of the spectrum. More details on this geometry are given in numerous sources such as Simpson et al. (1992) and Ostro (1993).

For most runs a frequency hopping technique was used whereby the transmitter frequency was stepped between four frequencies separated by 10 kHz and centered on 2380 MHz, with 10 s spent at each frequency step. This would allow measurement of the background noise at each of those frequencies at times when the echo was at one of the others, in the event of narrow or variable interference or other artifacts in the band. With no *a posteriori* apparent interference in the receiving band, we instead used a reduction procedure of fitting a polynomial to the regions outside the Titan spectrum which was then subtracted from the entire spectrum to give a normalized one in units of the standard deviation of the noise background. On a few days in 2007 the transmitter frequency was not stepped in order to facilitate detection of echoes from other saturnian satellites that were simultaneously

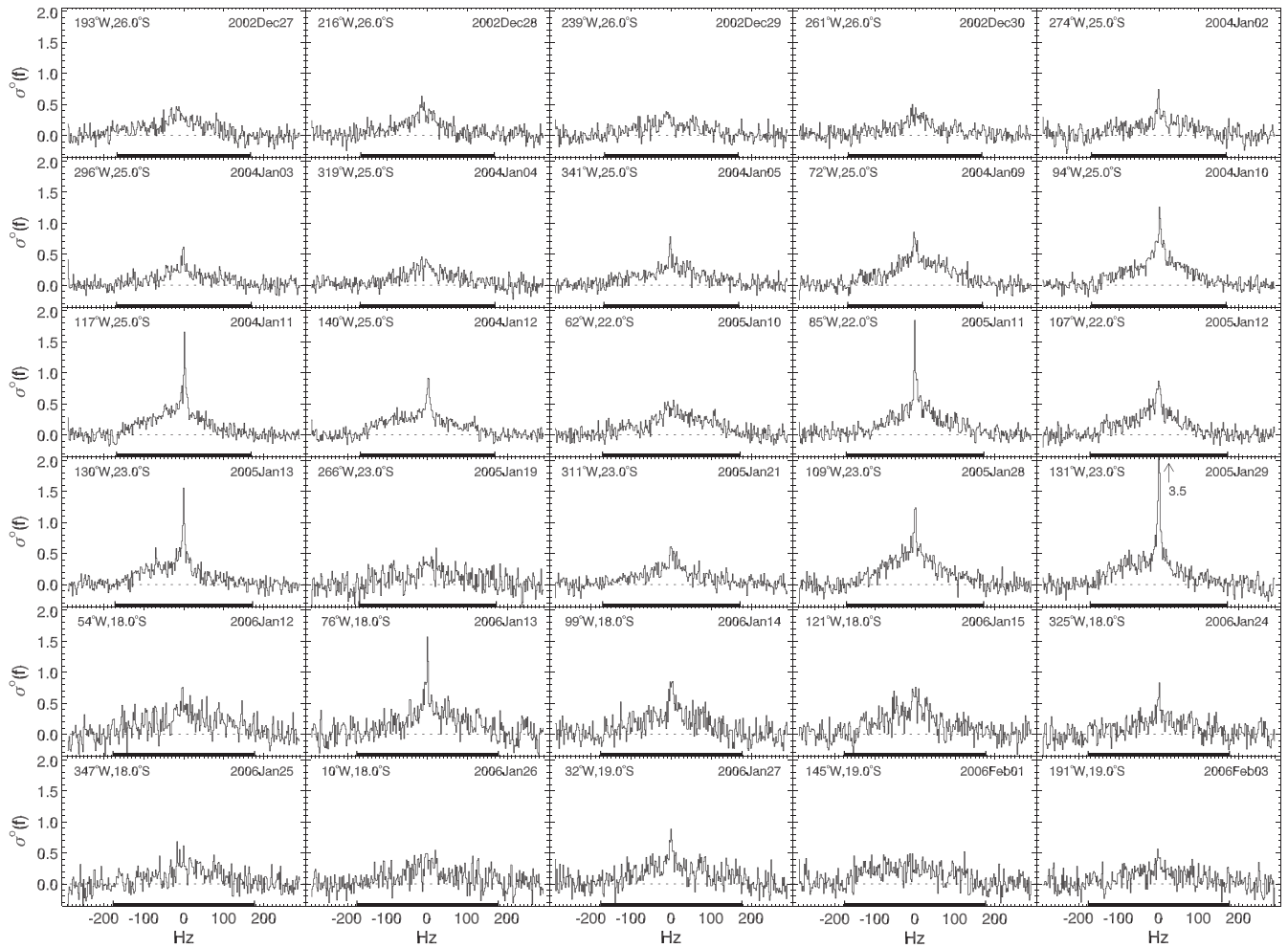


Fig. 2 (continued)

within the Arecibo beam with Titan, but at different, drifting frequencies. Those satellite observations have been reported in Black et al. (2007). On one date, 2002 December 21, an observation with a phase coded transmission was also successfully made as an attempt at a range measurement, but that is not included in the discussion here.

The system and observing parameters were then used to convert the spectra to physical cross section units, i.e. km^2 , which are then normalized by the projected surface area to produce a specific cross section per bin, $\sigma^0(f)$. Each spectrum was ultimately integrated over frequency to obtain a disk integrated specific radar cross section, $\hat{\sigma}$, referred to as the “radar albedo” for simplicity and which represents the total radar cross section normalized by the projected area of Titan’s disk. Further details of the reduction and normalization are given elsewhere (cf. Ostro, 1993; Ostro et al., 1992).

Tables 2 and 3 list the daily log of all observations. Each day’s run is reduced to a single spectrum in each polarization. The tables give the total echo strength obtained simply by summing the echo within the expected bandwidth of Titan on each day, expressed both as the raw signal-to-noise ratio (SNR) and as reduced to the radar albedo ($\hat{\sigma}$) in each polarization. The polarization ratio μ_C is formed from the ratio of the albedos as $\hat{\sigma}_{SC}/\hat{\sigma}_{OC}$. Table 2 lists the Arecibo observations. Since the calibration of both the GBT and Arecibo data in 2008 gave consistent results between the two, they have been weighted by their respective system parameters and

summed for those days when both systems received. GBT data obtained prior to 2008 had poor absolute calibration and has not been directly combined with the Arecibo data and are logged separately in Table 3 without reduced radar albedo estimates. The tables include the location of the sub-radar point of the center of the track, the integration time obtained (τ_{int}), and the round-trip light travel time (RTT).

The final daily OC spectra from Arecibo, including the 2008 GBT data, are shown in Fig. 2 and the corresponding SC spectra in Fig. 3. Spectra obtained with the GBT prior to 2008 are shown separately in Figs. 4 and 5.

3. Analysis

Fig. 6 shows the disk integrated radar albedos and circular polarization ratios estimated from each spectrum. Year to year values at the same longitude are quite consistent, supporting our sense that the system performance and calibration have remained similarly stable. Some scatter is likely due to the $\sim 18^\circ$ span of latitudes covered. Averaging the daily radar albedos as weighted by their individual statistical uncertainties gives average global values of 0.161 ± 0.001 for the OC radar albedo, 0.0736 ± 0.001 for the SC albedo, and 0.46 ± 0.07 for the polarization ratio. That the leading hemisphere is brighter than the global average is certainly due to the Xanadu region which is also more reflective than average in

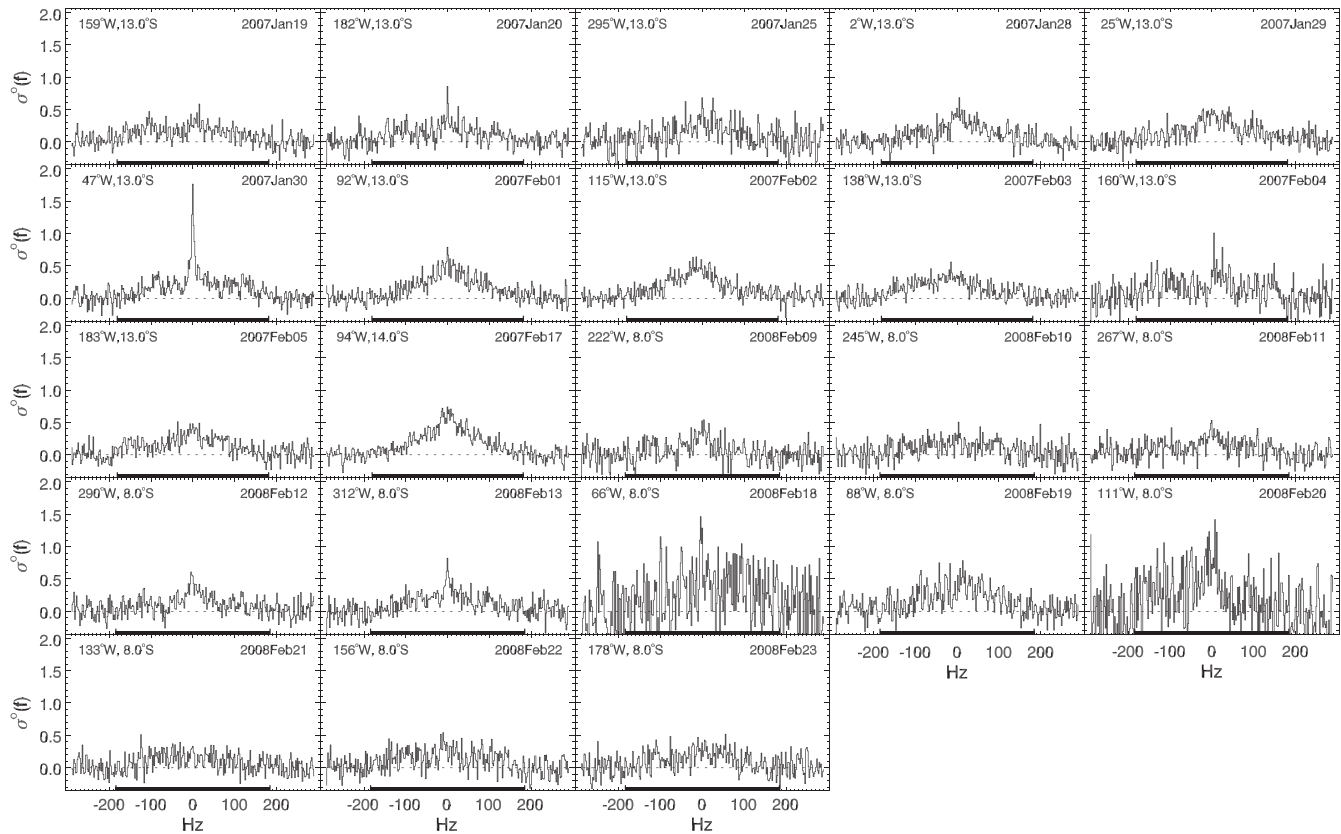


Fig. 2 (continued)

infrared bands (Barnes et al., 2007a). Overall, the trends in radar albedo versus longitude match quite well with the longitude variation in disk integrated infrared brightness (Buratti et al., 2006; Griffith et al., 1998), suggesting that the same components of the surface may be responsible for the behavior in both wavelength regimes (Campbell et al., 2003).

Inspection of the echo spectra in Figs. 2–5 suggests that they are composed of both specular and diffuse scattering components, with the diffuse component dominating the echo power. The specular component is a steeper and sometimes very narrow component that arises from single reflections off a surface relatively smooth on the wavelength scale. Such reflections have a strong incidence angle dependence and are most important where the surface incidence angles are nearly normal to the radar line-of-sight and thus the specular component manifests as a spike in reflectivity at the center of the OC echo spectrum which contains the contributions from the area around the sub-radar location. Furthermore, single reflections switch the polarization of a circular signal, and so the specular component only appears in the OC spectra. The diffuse echo is in a broad, relatively flat component that extends across the spectrum, resulting from wavelength-scale structure or multiple surface or volume scattering. Multiple scattering generally works to depolarize the signal, and thus this component appears in both polarizations and is less sensitive to incidence angle than the specular component.

Generically, the spectra shapes and albedos are not too dissimilar from those of inner Solar System targets such as the Moon, Mars, or Venus. The radar spectra of those objects are dominated by strong specular reflections as well as a broad diffuse component primarily from wavelength scale surface structure. That situation is a consequence of rocky, radar absorbing surfaces that are fairly smooth on larger scales but with some centimeter to meter scale

roughness. Average radar albedos for these objects are less than ~ 0.15 and their polarization ratios are of order 0.1–0.3 (cf. review by Ostro (1993)). In sharp contrast, very different scattering behavior is observed from other outer Solar System moons that have been observed with radar, namely the icy Galilean satellites and the smaller saturnian moons. These objects have surfaces predominantly of water ice which can be quite transparent to the radar signal (Thompson and Squyres, 1990) permitting sub-surface scattering effects to dominate. The result is that these objects have very high radar albedos, up to 2.5 for Europa, are completely dominated by diffuse echo from multiple scattering with little to no specular component, and have circular polarization ratios of order unity or higher (cf. Campbell et al., 1977; Ostro et al., 1992; Ostro et al., 2006; Black et al., 2007).

Although the dominant constituent of Titan's near-surface is also probably water ice (cf. (Grasset et al., 2000)), its radar albedos and polarization ratios are much lower than other radar detected icy moons, possibly indicating that the sub-surface multiple scattering thought to be the cause of the very high values is not working nearly as effectively on Titan. This difference could be due to a contaminant in Titan's surface that increases the radar absorptivity, or structural differences such that there are fewer sub-surface scattering centers necessary for an effective multiple scattering effect. However, the polarization ratios for Titan are of order 50%, which is intermediate between those of rocky-surface targets and icy-surface targets, suggesting that a multiple scattering effect mechanism is still fairly effective or there is an inhomogeneous mix of surfaces types with differing scattering properties on scales larger than the wavelength.

To the radar, Titan thus appears to be a hybrid. The low to moderate albedos and combined specular and diffuse scattering suggest a configuration dominated by surface scatter similar to the

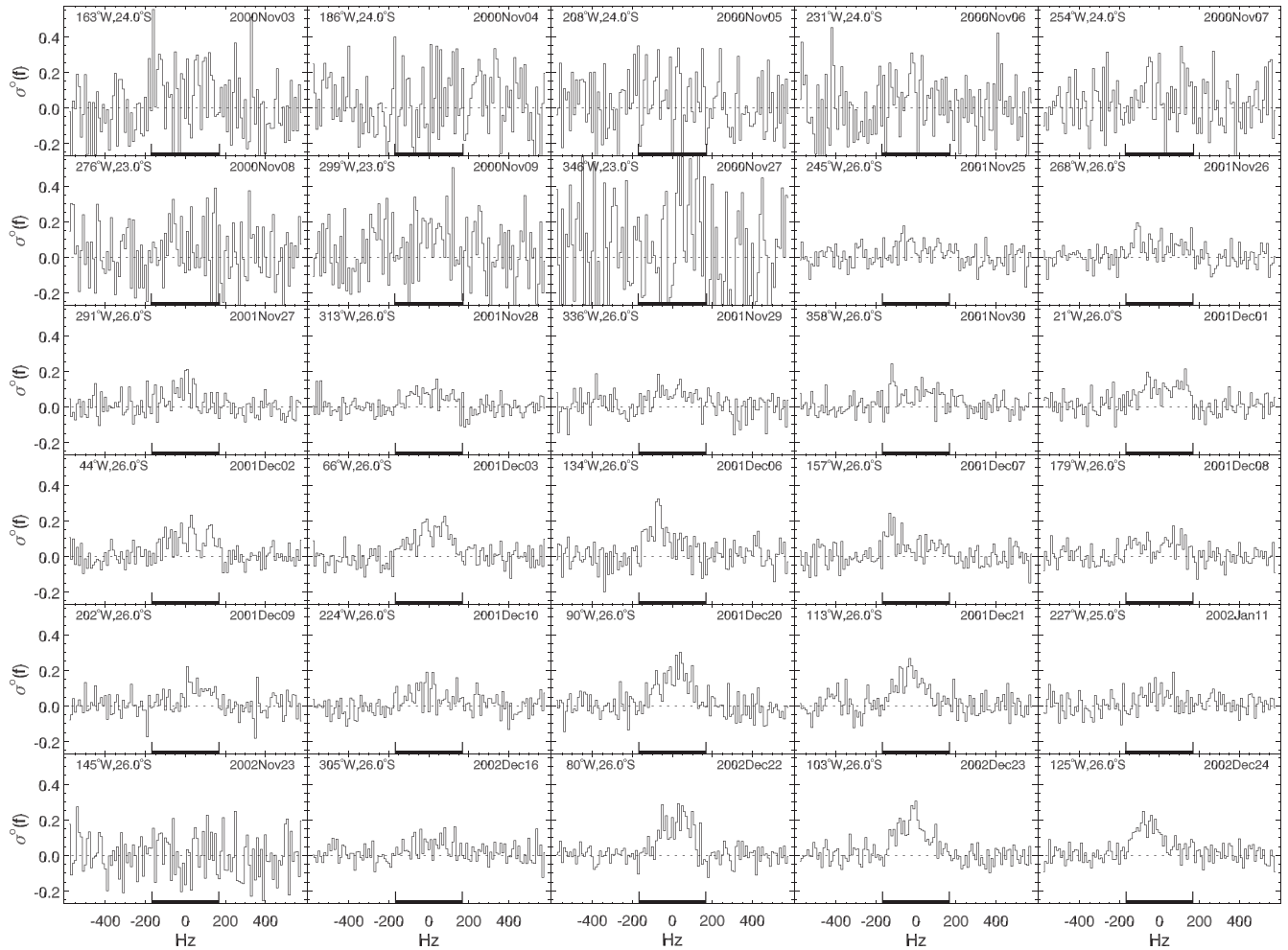


Fig. 3. Same as Fig. 2 but in the SC polarization channel. The frequency resolution is 10 Hz, which at the sub-radar location corresponds to ~ 140 km along the surface and incidence angles $\leq 1.5^\circ$ at the sub-radar location.

rocky surfaces of the inner Solar System, consistent with a surface of water ice heavily contaminated by more radar absorbing materials or inhomogeneous on large scales. On the other hand, Titan's specular components are not particularly strong relative to the diffuse components, and the circular polarization ratios are fairly high. This combination suggests that multiple scattering as might occur in the near sub-surface is contributing although not at the highest efficiency. The longitude variations in Fig. 6 are consistent with this perspective, especially regarding the feature Xanadu Regio centered around 90°W . Its higher brightness at infrared wavelengths compared to other areas is thought to be the result of its cleaner or fresher water ice covering (Barnes et al., 2007a). That scenario would also explain the increase in radar albedo and slight rise in circular polarization ratio over that region as cleaner water ice would exhibit more efficient sub-surface multiple scattering. Conversely, trailing hemisphere longitudes contain more infrared dark terrain and also have lower radar albedos and polarization ratios, both indicative of more non-ice material, more absorption, and less sub-surface scattering.

3.1. Scattering model

The echo spectra here are the sum of contributions from all scattering angles over the Earth-facing hemisphere at the time of observation, and so their shapes depend on the angular scattering function of the surface. There has been much work over nearly the

past half century to interpret the angular scattering behavior in terms of physical surface parameters, especially the specular component in terms of the reflectivity and wavelength-scale roughness (or smoothness) of the surface. For the terrestrial planets and the Moon, such reflections have been successfully described by the Hagfors scattering law (Hagfors, 1964),

$$\sigma_s^0(\theta) = \frac{1}{2} \frac{\rho C}{(\cos^4 \theta + C \sin^2 \theta)^{3/2}}, \quad (2)$$

which gives the specific cross section as a function of incidence angle θ dependent on the Fresnel reflectivity ρ and a roughness parameter C . C is typically considered to represent the root-mean-square (RMS) surface slope $\alpha = 1/\sqrt{C}$. For higher RMS surface slopes (increasing roughness), more power is reflected at angles away from normal incidence, increasing the angular width of the specular component in the spectrum. The normalization is such that a homogeneous object with scattering described with only this scattering law and typical RMS surface slopes of a few degrees or less would have a radar albedo of approximately ρ . Increasing the surface roughness will cause ρ to increasingly underestimate the true radar albedo. There have been other similar scattering functions used that are based on more realistic surface structure descriptions, some using scale dependent roughness parameters (e.g., Campbell, 2007; Sultan-Salem and Tyler, 2006). Wye et al. (2007) have used the Hagfors law as well as a Gaussian-based law to model Cassini

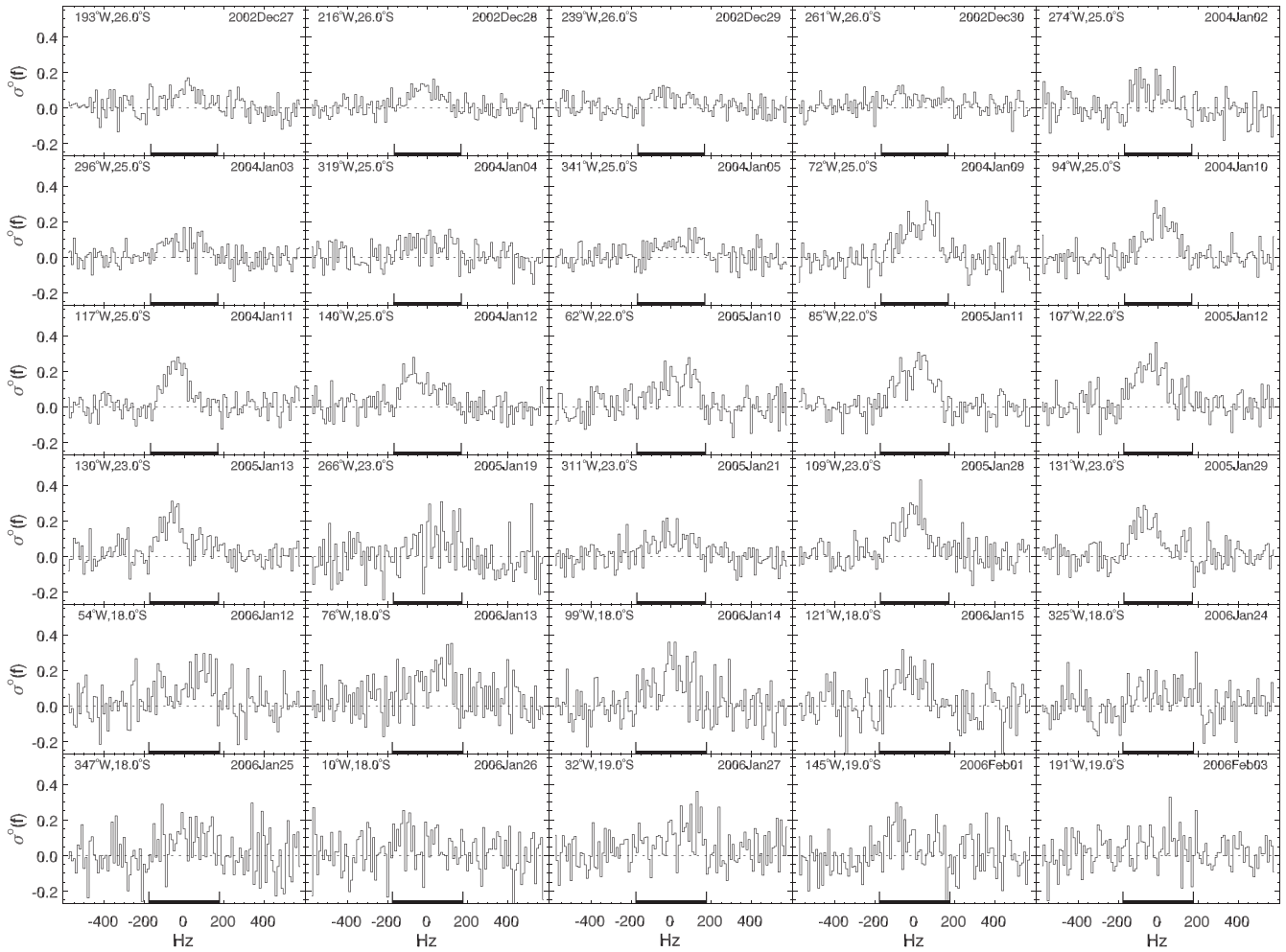


Fig. 3 (continued)

RADAR data. Given the moderate SNR of the spectra here, we will only use the standard Hagfors model as given by Eq. (2) to provide a basis for future efforts and also to connect to past work on other objects. A subset of these data was modeled by Sultan-Salem and Tyler (2007) using Hagfors and combinations of exponential and Gaussian functions. The various models gave comparable fits to the data and similar derived surface parameters. More detailed scattering functions may not be warranted at this stage due to the latitude ambiguity issue addressed later.

At higher incidence angles away from the sub-radar point and extending to Titan's limb, the spectra are modeled by the standard empirical diffuse scattering function:

$$\sigma_D^0(\theta) = A \frac{n+1}{2} \cos^n \theta. \quad (3)$$

This component represents high-order multiple scattering which works to depolarize the echo and cause a more gentle incidence angle dependence. The normalization makes A the radar albedo of a surface described by only this scattering law. Typical values of n for other objects fall between 1 and 2. Lommel-Seeliger scattering would be $n = 1$ such as the Earth's moon exhibits at optical wavelengths, and Lambert scattering would be $n = 2$. Multiple scattering could result from either surface roughness or sub-surface volume scattering, but these data do not discriminate these two possibilities well. Analysis of Cassini RADAR and emissivity data by Zebker et al. (2008) suggests that volume scatter dominates for Titan.

Each frequency of the one dimensional radar spectrum contains contributions from different locations on the surface that all have the same apparent Doppler shift but that also have different incidence angles. For a given scattering law dependent on incident angle, following Harmon et al. (1982) the measured radar spectrum will then be:

$$\sigma^0(f) = \frac{2}{\pi f_0} \int_{\sin^{-1}(f/f_0)}^{\pi/2} \frac{\sigma(\theta) \sin \theta}{(\sin^2 \theta - (f/f_0)^2)^{1/2}} d\theta, \quad (4)$$

where f_0 is the frequency of the limb and half the limb-to-limb bandwidth found earlier, $f_0 = B/2$.

To each OC spectrum we performed a least squares fit of Eq. (4) using the sum of Eqs. (2) and (3) for the scattering law with parameter set $\{\rho, C, A, n\}$. For each SC spectrum only Eq. (3) with parameter set $\{A, n\}$ was used. OC and SC spectra were fit independently. To obtain a starting parameter set, a fit to the weighted sum of all spectra was done. These total Titan spectra represent the average scattering properties of the entire surface, and are shown with their model fits in Fig. 7. For the total OC spectrum the best fit parameters are $\rho = 0.028 \pm 0.001$, $C = 474 \pm 29$ (or $\alpha = 2.63^\circ \pm 0.08^\circ$), $A = 0.132 \pm 0.001$, and $n = 2.29 \pm 0.06$. For the total SC spectrum the best fit parameters are $A = 0.074 \pm 0.001$ and $n = 1.27 \pm 0.07$.

Best fit parameters to each spectrum are shown as a function of longitude in Fig. 8. The Hagfors C parameter has been converted into RMS slope α . As expected, most of the OC echo can be

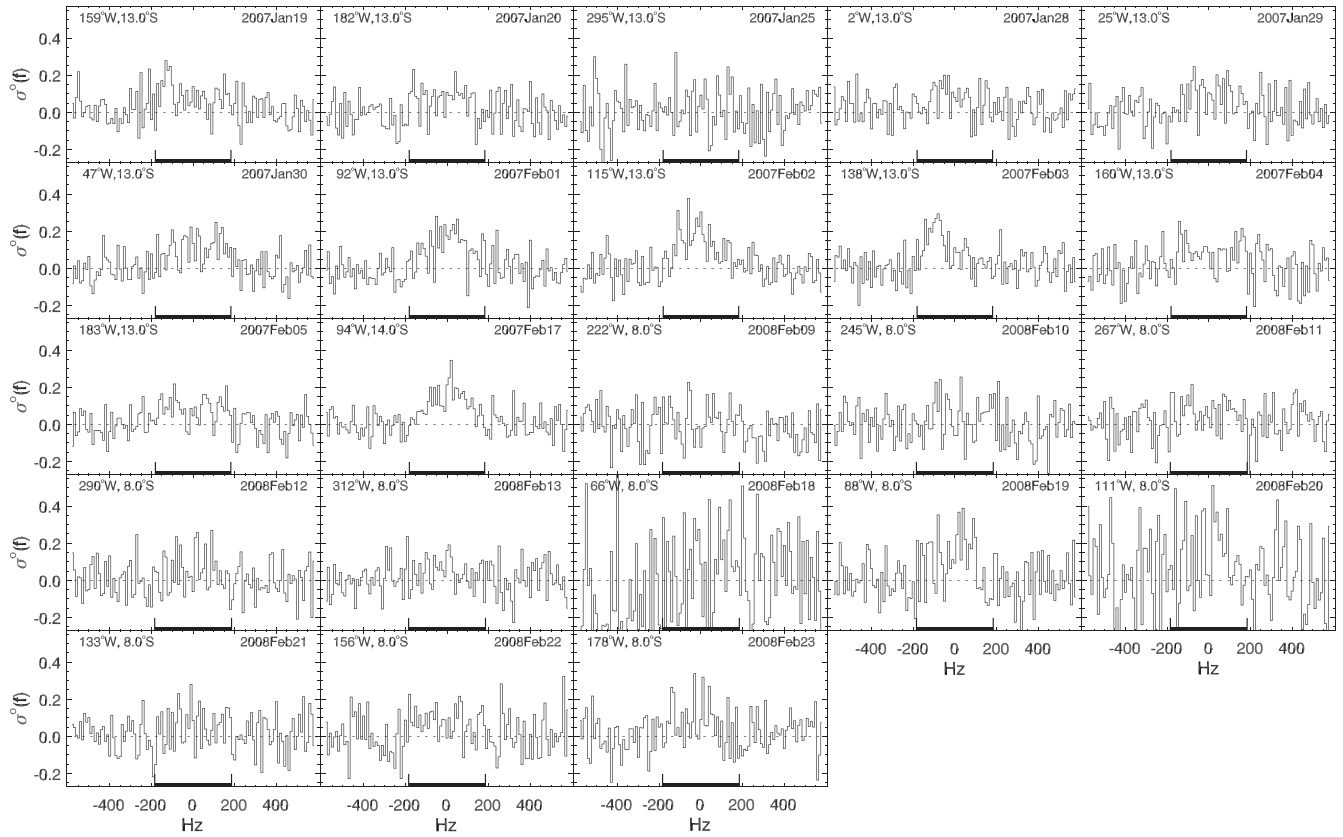


Fig. 3 (continued)

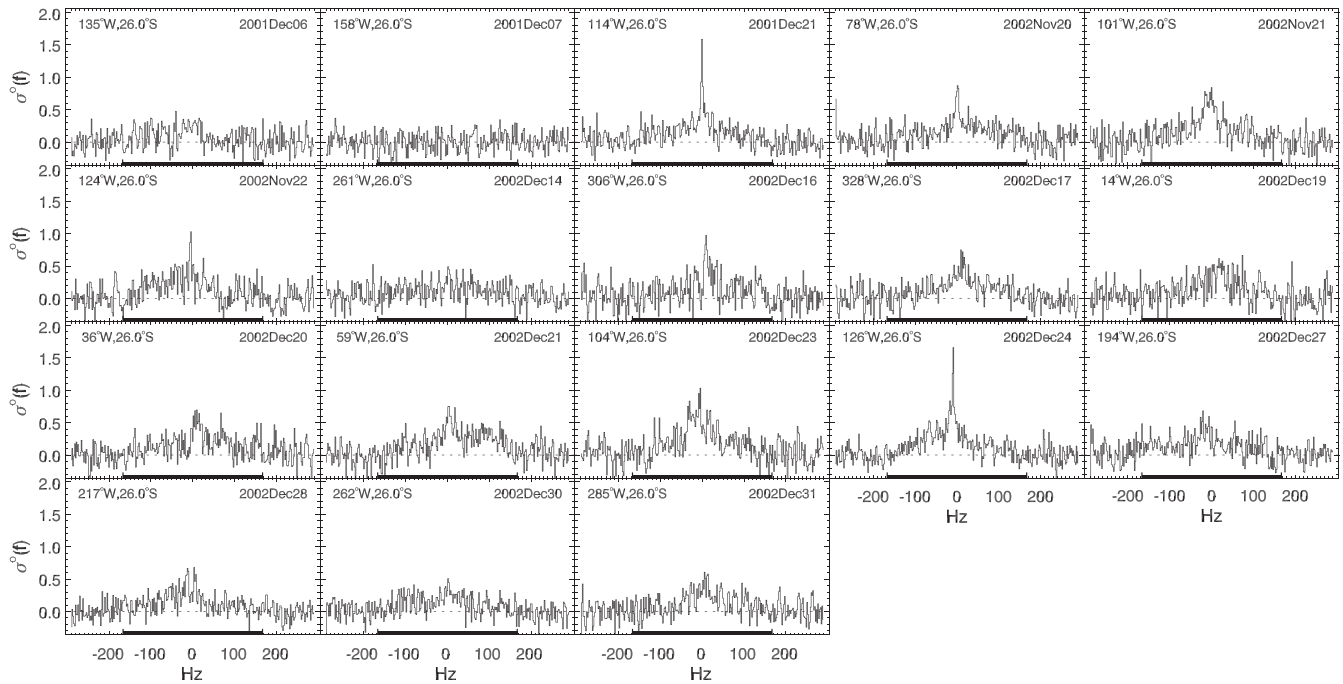


Fig. 4. Same style plot as Fig. 2 but of OC spectra obtained at the GBT on dates prior to the 2008 opposition. Due to possible calibration issues, these could not reliably be combined directly with the Arecibo data as could be done in 2008.

represented by the diffuse component, amplitude A , whose variation matches the disk integrated OC radar albedo versus longitude behavior (Fig. 6). As only a diffuse component is fit to the SC

spectra, its amplitude must track the SC radar albedo. The strength of the specular component, ρ , is roughly a quarter of the OC diffuse echo strength and only weakly tracks the radar albedo. The RMS

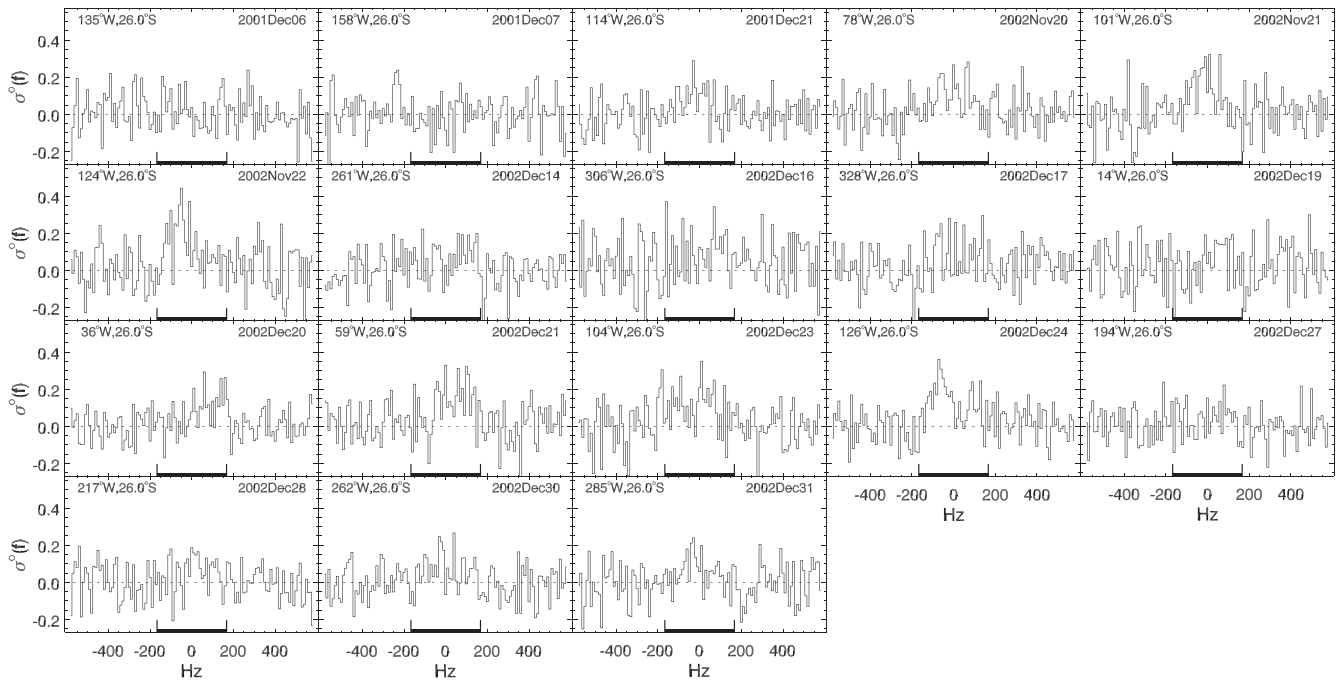


Fig. 5. Same as Fig. 4 but in the SC polarization channel. Resolution is 10 Hz.

slopes obtained from these spectra are significantly smaller than those measured at 2.2 cm wavelength by the Cassini RADAR (Wye et al., 2007). The larger RMS slopes at shorter wavelengths is consistent with the behavior of other surfaces such as the Moon (Hagfors, 1970) or Mars (Harmon et al., 1992).

That the n parameter which gives the shape of the diffuse scattering law shows considerable scatter is not surprising. If the visible hemisphere is comprised of terrains of differing reflectivities, even with the same n , the resulting echo spectrum may be poorly represented by a single scattering law. Such mixing is less of an issue for the specular component which is mainly sensitive to the center of the visible disk and hence less surface area. One manifestation of this mixing is that most of the echo spectra are in fact noticeably asymmetric. This effect is also easily noticeable when Xanadu is in view. For example, if Xanadu is in the center of the disk then the echo spectrum will have higher amplitude toward its center than at its sides, and application of the diffuse function will produce a seemingly centrally peaked fit, i.e., with higher n . Similarly, a broad specular component might be mis-identified as a diffuse component and contribute to an increase in the measured n , but since the same rise in n is generally seen in both polarizations, while the specular component only appears in the OC spectra, this is not a sufficient explanation for all the scatter in n .

The panels of Fig. 9 are scatter plots of some fit parameters against each other. There appears to be a weak correlation between the strength of the specular component and the RMS slopes, although the increasing errorbars at higher RMS slopes and high ρ makes a clear determination of any such trend speculative. The narrow specular echoes generally give better fits, which may simply result from those being less sensitive to asymmetric spectra than the broad specular fits are. Some of these results suggest that better fits could be obtained by including two specular components, one for a broad component and one for a more narrow component, although the SNR for most spectra makes systematic application of a double fit to the entire dataset difficult. Fig. 9 also shows the amplitude of the diffuse component from the two polarizations plotted against each other. These points are on average slightly above the line representing the global average polarization

ratio, $\mu_c = 0.46$, as expected since the low μ_c specular component has effectively been removed. While the points have some scatter they are grouped around their own mean ratio, 0.56, suggesting that the mechanism responsible for the diffuse component does not vary too much between different terrain units while the amplitude of the effect varies by a factor of ~ 2 . However, at the higher albedos the circular polarization does increase slightly on average as would be expected if multiple scattering efficiency improves. Comparison of other pairs of parameters against each other did not present any obvious trends.

3.2. Specular components

The specular components in the OC spectra appear highly variable depending on the position of the sub-radar location, as can be seen in the spectra themselves or the variability in the fit parameters ρ and C (or α). The specular component at times is very broad while often it is narrow, and at some times extremely narrow. This behavior can change dramatically from one day to the next, implying that the surface properties responsible for the specular component change dramatically over the 22.5° of rotation within 24 h, corresponding to a linear extent of ~ 1000 km.

Especially interesting are the extremely narrow components which are fit by Hagfors models with RMS slopes as low as 0.3°. The strongest and narrowest specular echo was obtained from 80.3°W, 26.3°S and is shown in Fig. 10 along with the result of the fit of the combined scattering law with parameters $\rho = 0.025 \pm 0.001$, $C = 9.7 \times 10^4 \pm 1.2 \times 10^4$ (or $\alpha_{rms} = 0.2^\circ \pm 0.1^\circ$), $A = 0.167 \pm 0.006$, and $n = 4.5 \pm 0.5$. This location is in the feature Hotei Regio on the southeast edge of Xanadu, and is suspected of being a cryovolcanic feature (Wall et al., 2009).

It had been proposed that hydrocarbon liquids, primarily methane, may exist on Titan (cf. Owen, 1982) because the surface temperature is near the condensation point of the methane occurring in the atmosphere at a few percent level, and that Titan may even have a methane cycle similar to Earth's water cycle (Atreya et al., 2006). While dynamics (Sears, 1995; Sagan and Dermott, 1982), the first infrared maps of the surface (Smith et al., 1996; Combes

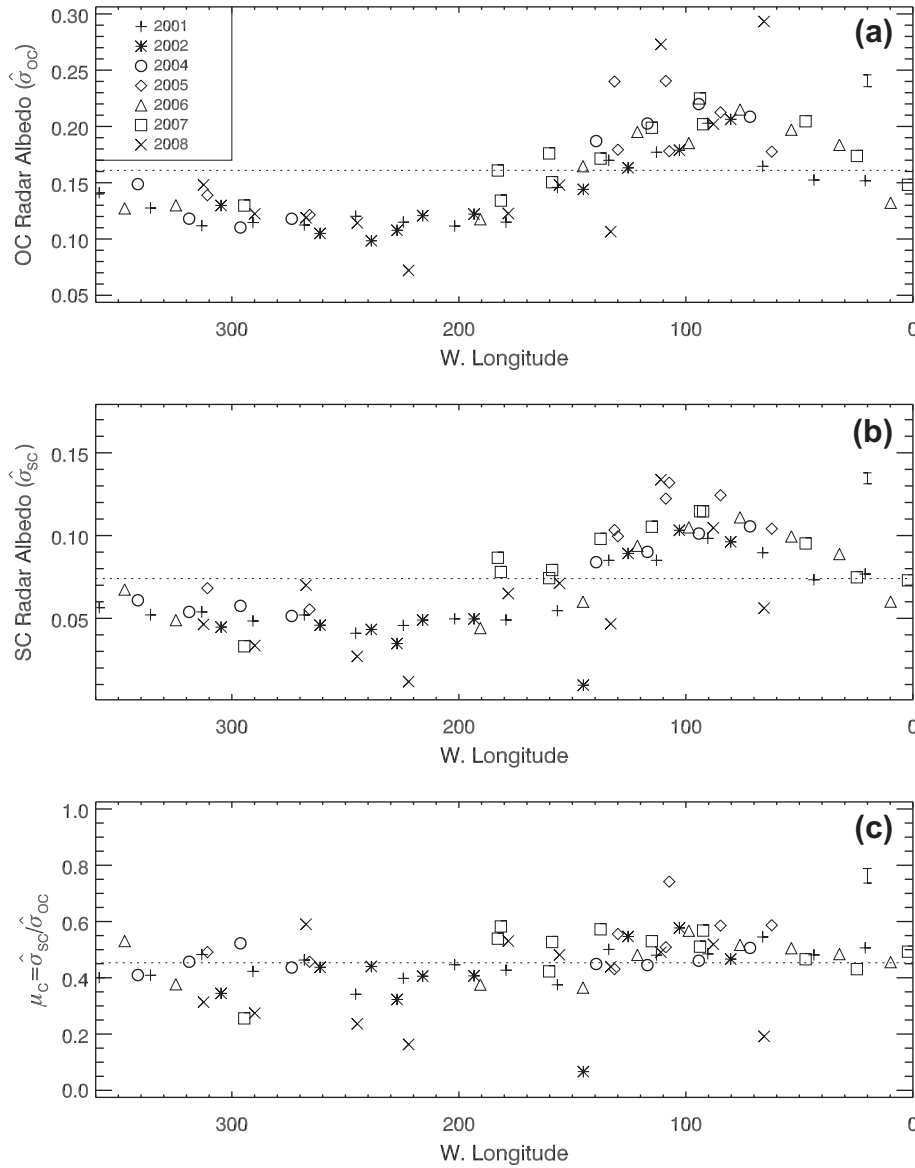


Fig. 6. Panels (a) and (b) plot the disk-integrated specific radar cross sections, a.k.a. the radar albedo, in the OC and SC polarizations, respectively, obtained by summing over the echo spectrum from each date. Only the Arecibo and Arecibo + GBT spectra shown in Figs. 2 and 3 have been used. Values from the 2000 session have lower SNR and considerably more scatter than other years and so have not been included here. Panel (c) plots the circular polarization ratio obtained from the same data. Typical error bars representing only the statistical uncertainties are indicated in the upper right corners. Horizontal dashed lines indicate the weighted means of all points. For synchronous rotation, longitudes 0–180°W are ‘leading’ and 180–360°W are ‘trailing’. Note the higher than average reflectivities centered on ~100°W corresponds to the longitudes of Xanadu Regio.

et al., 1997), and the first radar observations (Muhleman et al., 1995) effectively ruled out a global ocean, Cassini observations of drainage and flow features (Lorenz et al., 2008; Burr et al., 2009) and even lake-like features themselves (Stofan et al., 2007) have confirmed that this picture is generally correct. As first discussed by Campbell et al. (2003) using a subset of these ground-based radar data, a straightforward interpretation of the narrow echoes is that they are the expected to result from liquid bodies which can have arbitrarily flat surfaces given appropriately low wind excitation of waves.

The amplitude of the specular component in the Hagfors model can be directly interpreted as the Fresnel reflectivity of the surface, which in turn depends on the dielectric constant ϵ as:

$$\rho = \left(\frac{\sqrt{\epsilon} - 1}{\sqrt{\epsilon} + 1} \right)^2. \quad (5)$$

Table 4 lists results for those fits for which the amplitude of the specular component is significant by at least three standard deviations, and gives the specular fit parameters converted into dielectric constant and RMS slope. While accurate for a perfectly smooth dielectric, Eq. (5) will *underestimate* ϵ as the surface becomes roughened and power is removed from the specular component into the diffuse component. Thus, as ρ from our scattering model can only underestimate the true reflectivity, the derived estimates of the dielectric constants should be considered as lower bounds. Excluding the two outliers with dielectric constants greater than 4, the rest fall in the range 1.5–2.7 with a median of 1.9. Generally the lowest RMS slopes correspond to the lower dielectric constants in the range 1.5–2, which appear roughly correlated in Fig. 11. These low values are consistent with values reported for liquid hydrocarbons under Titan surface conditions (Paillou et al., 2008) considering that although the primary liquid component

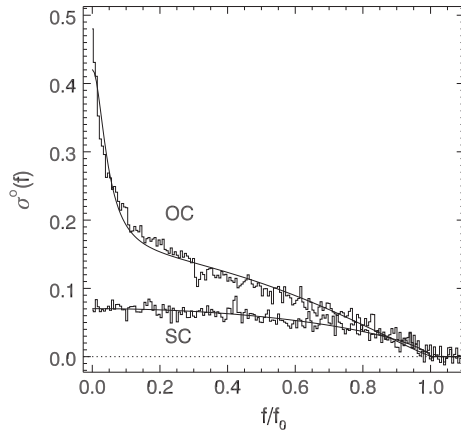


Fig. 7. The total weighted sum of all spectra from Figs. 2 and 3. Since these represent the average global properties, they have further been folded about the spectrum center and summed. Overplotted are fits of the Hagfors and diffuse (Eqs. (2) and (3)) scattering models to each. The abscissa has been normalized to f_0 , the frequency of Titan's limb. The parameters from these fits are listed in the text.

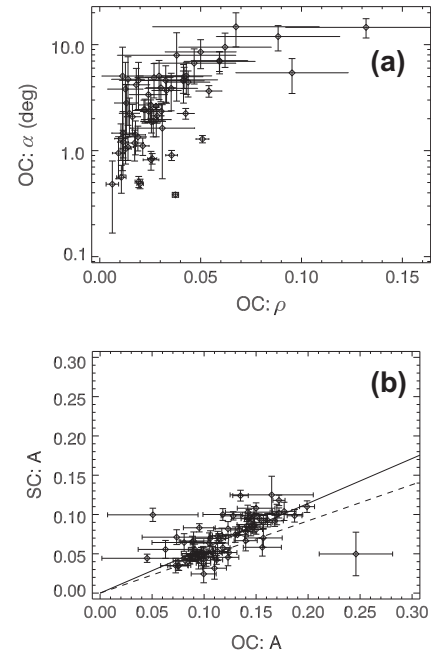


Fig. 9. Panel (a): fit parameters from the specular Hagfors model for reflectivity and RMS slope are plotted against each other, perhaps suggesting a weak correlation between these two parameters. Panel (b): diffuse amplitude from fits in both OC and SC channels for each spectrum are plotted against each other. The dashed line is the global average polarization ratio, $\mu_c = 0.46$, and the solid line is the average polarization ratio based only on this parameter, $\mu_c = 0.56$.

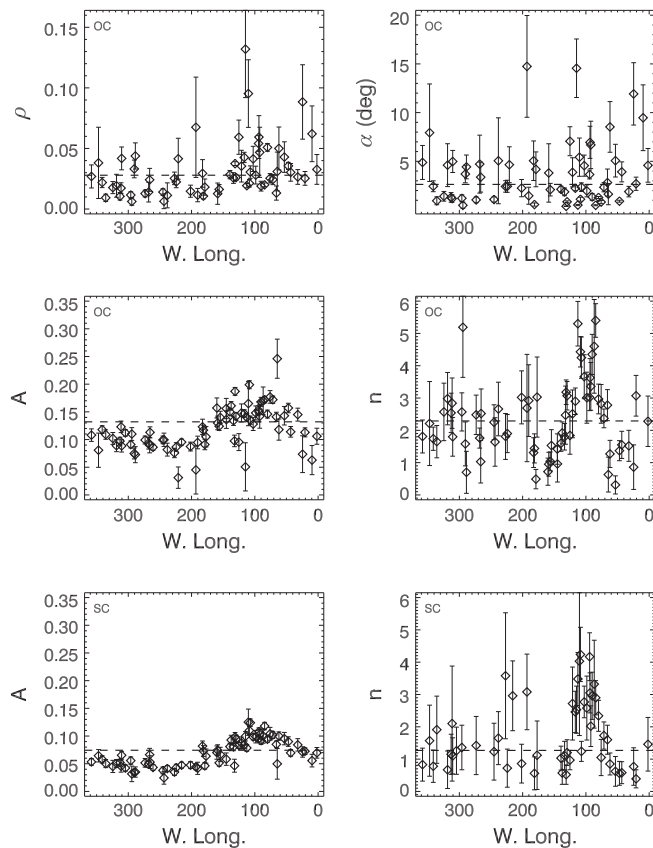


Fig. 8. Shown are the resulting parameters from fitting the Hagfors and diffuse models to each spectrum, each plotted as a function of sub-radar longitude. The top four panels are from the OC spectra, the lower two from the SC spectra. As expected, the amplitudes of the diffuse components A match the longitude variation in radar albedo seen in Fig. 6. Since each spectrum covers the entire Earth-facing hemisphere, each necessarily contains different terrain types with different scattering parameters. Thus a fit of a single scattering law to each sometimes has difficulty if those terrains are very different, which is likely contributing to much of the scatter and large uncertainties in these fits. The presence of the brighter than average Xanadu (centered on $\sim 100^\circ\text{W}$) noticeably distorts the spectra, causing much of the scatter in n values around that longitude. Horizontal lines are the parameters of the global average fit from Fig. 7.

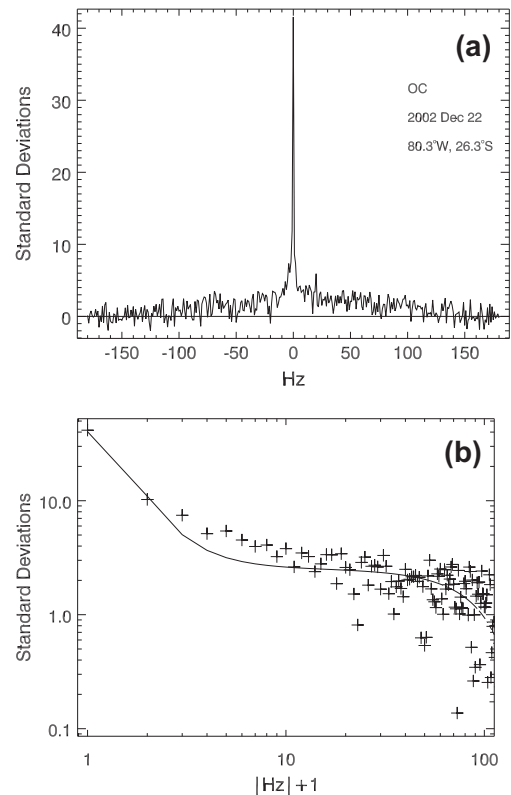


Fig. 10. Panel (a) shows the narrowest specular echo that was obtained. The frequency resolution is 1 Hz corresponding to ~ 14 km along the surface at the sub-radar point. Panel (b) shows the fit of the specular and diffuse scattering law to this spectrum, which has been folded in frequency and plotted on a logarithmic scale to better display the specular region. The frequency axis is slightly offset by one bin just to admit the zero frequency bin easily into the logarithm scale. There is a mismatch at ~ 5 – 10 Hz due to a feature at those positive frequencies.

Table 4

Parameters from specular fits.

Date (UTC)	Sub-radar point		ρ	C	ϵ	α_{rms} (°)
	W. Lon.	Lat.				
2001 December 01	21.0	−25.6	0.017 ± 0.003	2018 ± 909	1.7 ± 0.1	1.3 ± 0.3
2006 January 27	32.4	−18.5	0.026 ± 0.006	921 ± 526	1.9 ± 0.1	1.9 ± 0.5
2001 December 02	43.6	−25.6	0.029 ± 0.007	238 ± 124	2.0 ± 0.2	3.7 ± 1.0
2007 January 30	47.3	−13.2	0.036 ± 0.003	4005 ± 871	2.1 ± 0.1	0.9 ± 0.1
2006 January 12	53.5	−18.1	0.043 ± 0.013	127 ± 84	2.3 ± 0.3	5.1 ± 1.7
2004 January 09	71.7	−25.3	0.026 ± 0.004	498 ± 201	1.9 ± 0.1	2.6 ± 0.5
2006 January 13	76.1	−18.1	0.025 ± 0.004	4895 ± 1976	1.9 ± 0.1	0.8 ± 0.2
2002 December 22	80.3	−26.3	0.025 ± 0.001	97049 ± 12246	1.9 ± 0.1	0.2 ± 0.1
2005 January 11	84.7	−22.5	0.020 ± 0.002	13825 ± 2865	1.8 ± 0.1	0.5 ± 0.1
2001 December 20	90.3	−25.5	0.019 ± 0.004	1719 ± 900	1.7 ± 0.1	1.4 ± 0.4
2007 February 17	93.8	−13.9	0.059 ± 0.018	68 ± 32	2.7 ± 0.4	6.9 ± 1.7
2004 January 10	94.3	−25.3	0.043 ± 0.005	494 ± 121	2.3 ± 0.1	2.6 ± 0.3
2006 January 14	98.7	−18.1	0.028 ± 0.007	851 ± 532	2.0 ± 0.2	2.0 ± 0.6
2002 December 23	102.8	−26.3	0.036 ± 0.008	241 ± 111	2.2 ± 0.2	3.7 ± 0.9
2005 January 12	107.3	−22.5	0.031 ± 0.005	594 ± 222	2.0 ± 0.1	2.3 ± 0.4
2005 January 28	108.8	−22.9	0.021 ± 0.003	2674 ± 998	1.8 ± 0.1	1.1 ± 0.2
2008 February 20	111.0	−8.0	0.095 ± 0.028	111 ± 80	3.6 ± 0.7	5.4 ± 2.0
2001 December 21	113.0	−25.5	0.019 ± 0.002	12639 ± 3056	1.7 ± 0.1	0.5 ± 0.1
2007 February 02	115.0	−13.4	0.132 ± 0.040	15 ± 6	4.6 ± 1.2	14.6 ± 3.0
2004 January 11	116.9	−25.4	0.023 ± 0.002	6299 ± 1328	1.9 ± 0.1	0.7 ± 0.1
2002 December 24	125.5	−26.3	0.020 ± 0.002	4699 ± 1384	1.8 ± 0.1	0.8 ± 0.1
2005 January 13	129.9	−22.5	0.026 ± 0.002	4628 ± 1050	1.9 ± 0.1	0.8 ± 0.1
2005 January 29	131.4	−22.9	0.038 ± 0.002	22338 ± 2346	2.2 ± 0.1	0.4 ± 0.1
2001 December 06	134.0	−25.6	0.025 ± 0.004	950 ± 408	1.9 ± 0.1	1.9 ± 0.4
2004 January 12	139.5	−25.4	0.025 ± 0.003	1262 ± 355	1.9 ± 0.1	1.6 ± 0.2
2001 December 07	156.6	−25.6	0.014 ± 0.004	1089 ± 674	1.6 ± 0.1	1.7 ± 0.5
2007 January 20	181.5	−12.9	0.011 ± 0.002	10418 ± 6133	1.5 ± 0.1	0.6 ± 0.2
2001 December 09	201.8	−25.6	0.007 ± 0.002	11881 ± 8416	1.4 ± 0.1	0.5 ± 0.2
2002 December 28	215.9	−26.3	0.088 ± 0.017	29 ± 10	3.4 ± 0.4	10.5 ± 1.8
2001 December 10	224.5	−25.6	0.022 ± 0.005	597 ± 305	1.8 ± 0.1	2.3 ± 0.6
2002 January 11	227.2	−25.5	0.025 ± 0.004	902 ± 379	1.9 ± 0.1	1.9 ± 0.4
2001 November 25	245.5	−25.6	0.014 ± 0.003	3154 ± 1566	1.6 ± 0.1	1.0 ± 0.3
2004 January 02	273.6	−25.2	0.013 ± 0.003	2929 ± 1632	1.6 ± 0.1	1.1 ± 0.3
2008 February 12	289.9	−7.7	0.044 ± 0.011	167 ± 92	2.3 ± 0.3	4.4 ± 1.2
2001 November 27	290.7	−25.6	0.029 ± 0.006	342 ± 167	2.0 ± 0.2	3.1 ± 0.8
2004 January 03	296.2	−25.2	0.009 ± 0.002	6756 ± 3704	1.5 ± 0.1	0.7 ± 0.2
2002 December 16	304.7	−26.2	0.014 ± 0.002	16473 ± 5492	1.6 ± 0.1	0.4 ± 0.1
2005 January 21	310.8	−22.7	0.042 ± 0.009	132 ± 60	2.3 ± 0.2	5.0 ± 1.1
2008 February 13	312.5	−7.7	0.017 ± 0.004	2359 ± 1527	1.7 ± 0.1	1.2 ± 0.4
2001 November 28	313.3	−25.6	0.010 ± 0.003	2209 ± 1654	1.5 ± 0.1	1.2 ± 0.5
2006 January 24	324.7	−18.4	0.018 ± 0.005	1653 ± 1166	1.7 ± 0.1	1.4 ± 0.5
2001 November 29	335.8	−25.6	0.010 ± 0.003	2849 ± 2414	1.5 ± 0.1	1.1 ± 0.5
2004 January 05	341.4	−25.2	0.014 ± 0.002	3257 ± 1387	1.6 ± 0.1	1.0 ± 0.2

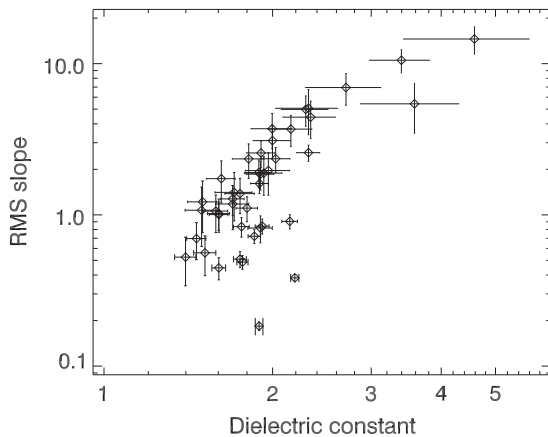


Fig. 11. Dielectric constants derived by applying Eq. (5) to the specular fit parameters are plotted versus RMS slopes estimated from the same fits. Only points for which the specular fit amplitudes ρ are significant at the level of three standard deviations are used. The range of dielectric constants spans that expected from solid and liquid hydrocarbons, and the fits suggest that the lower values, indicative of liquids, occur for the flattest areas (lowest RMS slopes) also.

on Titan is likely methane and ethane and perhaps propane (Cor-dier et al., 2009), identification of other components and their fractions are unknown but possibly important in setting the dielectric constant of their mixture. These dielectric constants and especially the higher ones could also be consistent with solid hydrocarbons, $\epsilon \sim 2\text{--}3$ (Thompson and Squyres, 1990), and water ice with a high enough porosity to reduce its dielectric constant from a value of 3.1 when solid (Warren, 1984). Overall, the low values from the model fits suggest a surface covered in low dielectric simple organic solids or liquids or one with a high degree of porosity, and one with a generally rough surface but with occasional very smooth areas.

Lake features observed in Cassini SAR imagery (Stofan et al., 2007) have sizes ranging from ~ 3 km to ~ 100 km, comparable to the length of the track of the sub-radar point in these ground-based data. To test for any such short length variability in these narrow specular components, the daily runs were reprocessed in shorter segments, although still long enough so as to maintain a useful signal level. For Arecibo and GBT data the time intervals were chosen to be 4 min and 20 min respectively. Selected Arecibo dates containing strong specular echoes are shown in Fig. 12, where plotted versus time is the strength of the echo in the central 5 Hz of the total spectrum which covers $\sim 0.77^\circ$ of longitude or

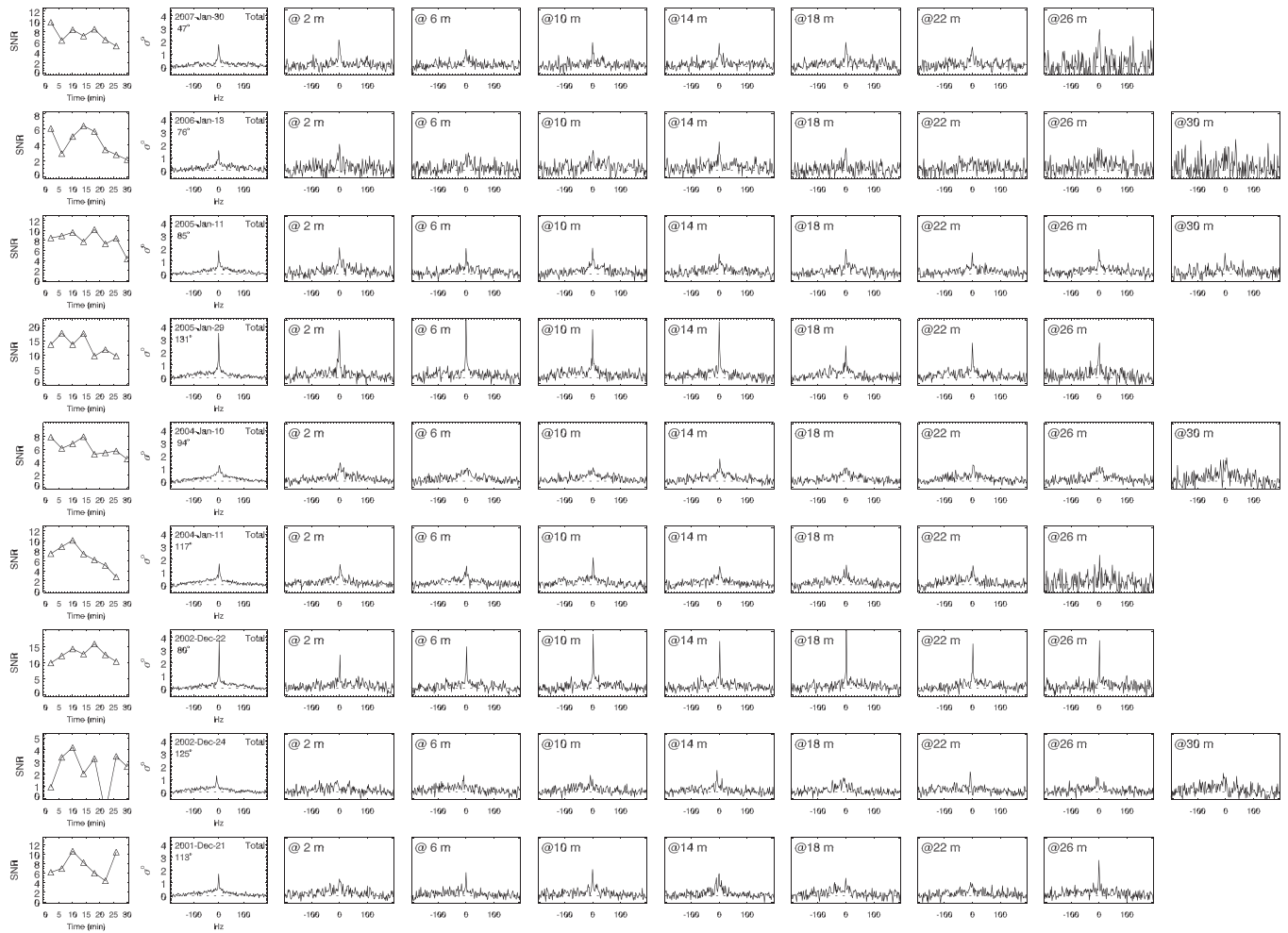


Fig. 12. Arecibo spectra for which there are narrow specular components are shown broken into smaller time intervals. The first column plots the SNR in the central 5 Hz versus time. The second column gives the total OC spectrum from each date, reproducing the same panels from Fig. 2. The remaining panels show the data from the central narrow specular components, with some changing substantially over several minutes or disappearing at times altogether. Four minutes corresponds to a track $\sim 0.06^\circ$ or ~ 2.7 km long. The last spectrum in each series is often noisier because it contains less than the full 4 min or was obtained at high zenith angles where Arecibo's performance worsens slightly.

~ 30 km, followed by the individual 4 min interval spectra. Fig. 13 shows similar reprocessing of those long GBT tracks from 2001 and 2002 which yielded a central echo of at least three standard deviations of the noise in at least one interval. Most of these narrow specular echoes show statistically significant variation over 2–3 intervals, implying an important change in surface type or properties during that period. Time intervals of 10–20 min of time correspond to 7–14 km, which must then be roughly the scale of the areas responsible for some of the rapidly variable specular echoes.

3.3. Isolation in longitude

As mentioned previously, the effectiveness of the fit procedure is limited by use of a single parameter set to describe an entire spectrum that includes the whole visible hemisphere of Titan and is certainly composed of different terrains with different radar properties. By simultaneously fitting to echo spectra taken at different orientations one could better reconstruct a rough map of the parameters over the surface. Ideally these different orientations would have sub-radar points evenly and completely distributed at sufficient intervals in both longitude and latitude. Unfortunately, the Earth–Titan geometry restricts the achievable

latitude span to only $\sim 20^\circ$. On the other hand, as Titan rotates 22.5° per day regular observations over a full rotation period, for example every day, will produce a series of spectra with sub-radar points evenly sampled in longitude. Such a series could be disentangled to better isolate the terrain at a particular sub-radar longitude although still containing latitudinal ambiguities. For example, the area around the sub-radar point on a given day will appear at the center of that day's echo spectrum, but at different spectral locations on other days. As a rough solution to better isolate that area from different terrain types at other longitudes, one might sort the spectra so as to select the location corresponding to that area from each spectrum and then fit to this reconstructed single-longitude spectrum. A similar sorting reconstruction algorithm has been used previously, for example with range-Doppler observations of Mars (Downs et al., 1973). The limitation of this technique is that with only one sub-radar latitude tracked, such an effort is complicated by the inclusion of areas at latitudes off the sub-radar track (which is not too far from the equator for the geometries here). These high latitude areas will track through the series of echo spectra differently than areas near the equator but at the same longitudes. This limitation should be mitigated by the scattering laws and geometry, in that those higher latitude areas are also at larger incidence angles and thus contribute less

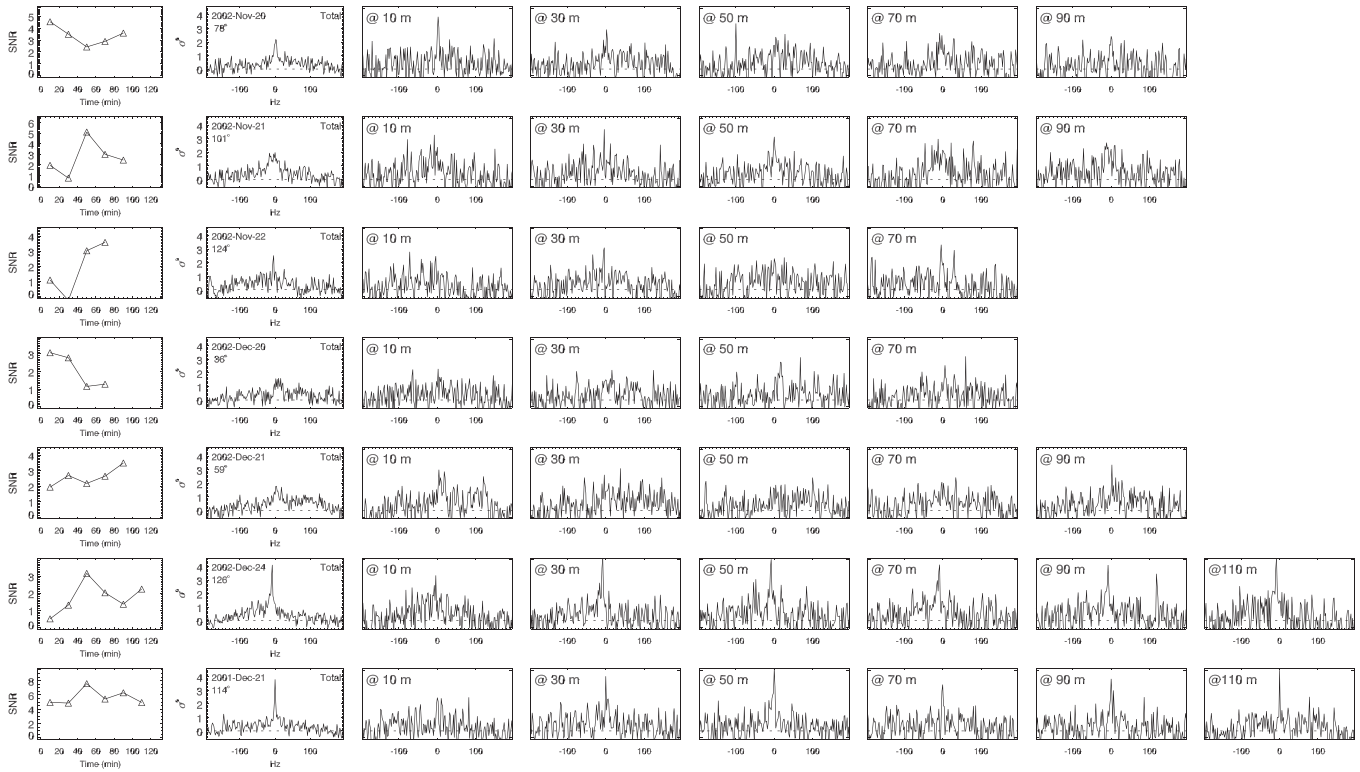


Fig. 13. The longer track GBT spectra are shown broken into smaller time intervals, using the same procedure as in Fig. 12 but here with 20 min intervals corresponding to surface tracks $\sim 0.3^\circ$ or ~ 13 km long.

to the echo spectra than areas near the sub-radar track. The echo spectra can then be considered to be weighed more toward the terrains around the sub-radar track, although clearly situations with a radar-dark equatorial region and radar-bright higher latitude regions will give ambiguous results at best.

The observing sessions at oppositions 2000–2002 were scheduled so as to measure the echo spectra at evenly spaced intervals covering an entire Titan rotation. Days were occasionally lost due to transmitter downtime and other equipment problems, and only in the 2001 opposition session did we obtain a regular uninterrupted series in longitude. Thus for now we restrict this reconstruction technique to the 16 spectra from 2001 as an initial step. Future work could include all spectra and a more rigorous remapping algorithm, and the small latitude span of the multi-year data set should somewhat help in resolving those latitude ambiguities.

Panel (a) of Fig. 14 shows the 16 spectra from the 2001 session stacked vertically to create an image. The ordinate is the longitude of the sub-radar point or the center of the spectrum. The higher reflectivity of the Xanadu region centered around $\sim 100^\circ$ W longitude can be seen appearing on the limb in the spectrum centered at roughly $\sim 0^\circ$ W, crossing the disk, and disappearing on the opposite limb in the spectrum centered at roughly $\sim 180^\circ$ W. A point on the sub-radar track at longitude λ_p will track through this image at a frequency position according to

$$f_p(\lambda) = f_0 \sin(\lambda - \lambda_p), \quad (6)$$

where λ is the current sub-radar longitude and the point is only visible if $|\lambda - \lambda_p| \leq 90^\circ$. The sorting of these spectra is an operation done on the spectra array in which each frequency bin is shifted in the longitude direction by an amount given by the inverse of Eq. (6), namely $\Delta\lambda = \sin^{-1} f/f_0$. This is exact for points on the sub-radar track although not for higher latitudes, which is the same

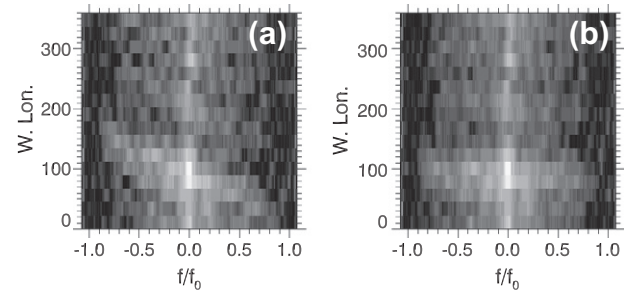


Fig. 14. Arecibo OC spectra from 2001 stacked and plotted as a grayscale image. These 16 spectra are equally spaced in longitude. The ordinate is the longitude of the sub-radar point, corresponding to the central bin of each spectrum. Spectra have been smoothed to 10 Hz resolution for illustration only. Panel (a) shows the original spectra, in which features would track through the spectra as Titan rotated under the sub-radar point. The feature crossing the sub-radar point ($f/f_0 = 0$) at $\sim 100^\circ$ W longitude is Xanadu. Panel (b) shows the same data after applying the shift from Eq. (6) to better align echoes from different spectra back to their originating longitude (see text). Panel (b) better isolates the scattering from a single longitude, with the dominant contribution coming from near the sub-radar location.

limitation discussed previously. The result of this shifting process is shown in panel (b) of Fig. 14, where now each reconstructed spectrum should contain echo mostly from a single longitude on the sub-radar track, as can be seen by the restriction of the bright Xanadu feature to a narrow band around its central longitude. Having spectra spaced equidistant in sub-radar longitude simplifies this process by avoiding any interpolation or averaging of spectra.

The same functions from Eqs. (2) and (3) are now fit to the reconstructed spectra from the 2001 session, with the results plotted in Figs. 15 and 16. The fit parameters to these spectra before and after the reconstruction are also listed in Table 5. The parameter ranges show less scatter. Most notably the rise in the diffuse

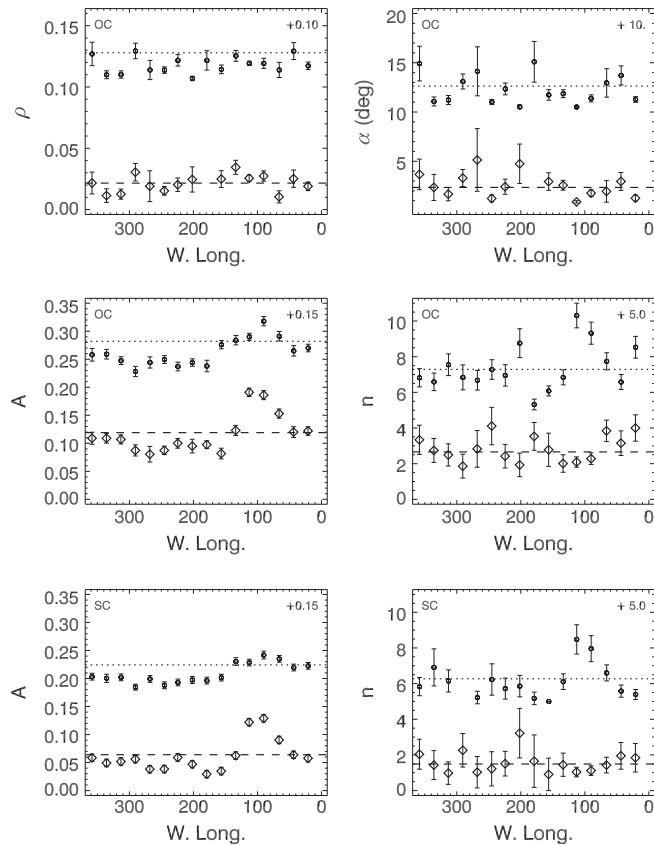


Fig. 15. Parameters from fitting the Hagfors and diffuse laws to the re-aligned spectra of Fig. 14. The alignment produces more symmetric spectra and fits with less scatter. The higher amplitude albedo Xanadu region is better constrained in longitude and since the spectra are now more symmetric the diffuse component in particular is better defined as shown by the reduced scatter in n . The original values from the fits done prior to the re-alignment are reproduced from Fig. 8 with smaller symbols and an upward vertical displacement (as indicated) for comparison to the fit parameters after re-alignment.

amplitude across Xanadu is now more constrained to match Xanadu's actual longitudes, and the scatter and high values of n have been mostly eliminated. Using the average of the two fits that straddle 100°W longitude, the average radar albedos for Xanadu are higher than the global averages, 0.22 ± 0.01 in OC and

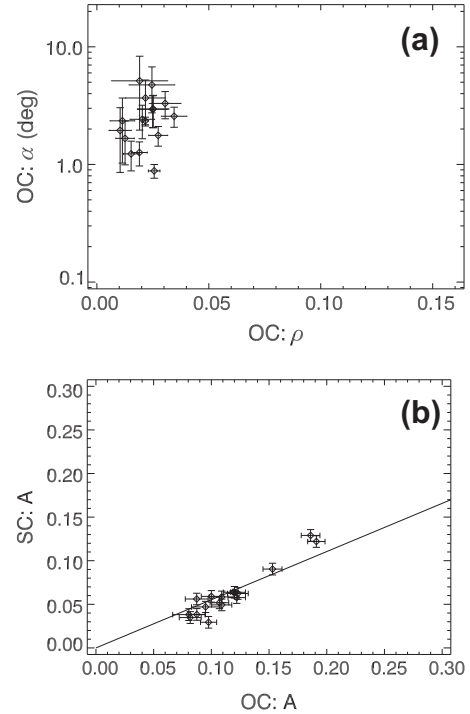


Fig. 16. Same as Fig. 9 but using the fit parameters from the re-aligned spectra of Fig. 14 only. The weak correlation in specular reflectivity versus RMS slope is less apparent in this subset but still appears if the one low point is ignored, and the diffuse amplitudes are much more tightly aligned.

0.13 ± 0.01 in SC, giving a polarization ratio of 0.59 ± 0.05 , consistent with it being a region of relatively cleaner water ice. For the trailing hemisphere to the average OC radar albedo is 0.12 ± 0.01 , average SC radar albedo is 0.05 ± 0.01 , giving an average circular polarization ratio of 0.42 ± 0.09 .

3.4. Comparison with Cassini SAR imagery

The properties of at least some of the specular echoes, namely low cross sections and very small RMS slopes, are consistent with reflections from liquid hydrocarbon surfaces. Despite the quite convincing discovery with the Cassini RADAR of lakes only at high latitudes (Stofan et al., 2007) including a specular glint from

Table 5
Parameters from 2001 spectra before and after longitude rebinning.

Lon. (deg)	Original spectra				Rebinned spectra			
	ϵ	$\alpha_{rms} (^{\circ})$	A	n	ϵ	$\alpha_{rms} (^{\circ})$	A	n
21.0	1.7 ± 0.1	1.3 ± 0.3	0.12 ± 0.01	3.5 ± 0.6	1.7 ± 0.1	1.3 ± 0.3	0.12 ± 0.01	4.0 ± 0.7
43.6	2.0 ± 0.2	3.7 ± 1.0	0.12 ± 0.01	1.6 ± 0.4	1.9 ± 0.2	3.0 ± 0.9	0.12 ± 0.01	3.2 ± 0.7
66.2	1.6 ± 0.2	3.0 ± 1.4	0.14 ± 0.01	2.7 ± 0.5	1.5 ± 0.3	1.9 ± 1.1	0.15 ± 0.01	3.8 ± 0.6
90.3	1.7 ± 0.1	1.4 ± 0.4	0.17 ± 0.01	4.3 ± 0.6	2.0 ± 0.1	1.8 ± 0.3	0.19 ± 0.01	2.3 ± 0.3
113.0	1.7 ± 0.0	0.5 ± 0.1	0.14 ± 0.01	5.3 ± 0.7	1.9 ± 0.1	0.9 ± 0.1	0.19 ± 0.01	2.1 ± 0.3
134.0	1.9 ± 0.1	1.9 ± 0.4	0.13 ± 0.01	1.8 ± 0.4	2.1 ± 0.1	2.6 ± 0.5	0.12 ± 0.01	2.0 ± 0.5
156.6	1.6 ± 0.1	1.7 ± 0.5	0.13 ± 0.01	1.1 ± 0.3	1.9 ± 0.2	2.9 ± 0.9	0.08 ± 0.01	2.8 ± 0.9
179.2	1.8 ± 0.2	5.1 ± 2.1	0.09 ± 0.01	0.3 ± 0.3	–	–	0.10 ± 0.01	3.5 ± 0.8
201.8	1.4 ± 0.1	0.5 ± 0.2	0.09 ± 0.01	3.8 ± 0.8	1.9 ± 0.2	4.7 ± 2.0	0.09 ± 0.01	1.9 ± 0.7
224.5	1.8 ± 0.1	2.3 ± 0.6	0.09 ± 0.01	2.0 ± 0.6	1.8 ± 0.1	2.4 ± 0.8	0.10 ± 0.01	2.4 ± 0.7
245.5	1.6 ± 0.1	1.0 ± 0.3	0.10 ± 0.01	2.3 ± 0.6	1.6 ± 0.1	1.2 ± 0.3	0.09 ± 0.01	4.1 ± 1.0
268.1	1.6 ± 0.2	4.1 ± 2.5	0.09 ± 0.01	1.7 ± 0.6	1.7 ± 0.5	5.1 ± 3.2	0.08 ± 0.01	2.8 ± 1.0
290.7	2.0 ± 0.2	3.1 ± 0.8	0.08 ± 0.01	1.8 ± 0.7	2.0 ± 0.2	3.3 ± 0.9	0.09 ± 0.01	1.9 ± 0.7
313.3	1.5 ± 0.1	1.2 ± 0.5	0.10 ± 0.01	2.5 ± 0.6	1.6 ± 0.1	1.7 ± 0.7	0.11 ± 0.01	2.5 ± 0.6
335.8	1.5 ± 0.1	1.1 ± 0.5	0.11 ± 0.01	1.6 ± 0.5	1.5 ± 0.2	2.3 ± 1.3	0.11 ± 0.01	2.7 ± 0.7
358.4	1.9 ± 0.2	4.9 ± 1.8	0.11 ± 0.01	1.8 ± 0.5	1.8 ± 0.2	3.7 ± 1.6	0.11 ± 0.01	3.3 ± 0.8

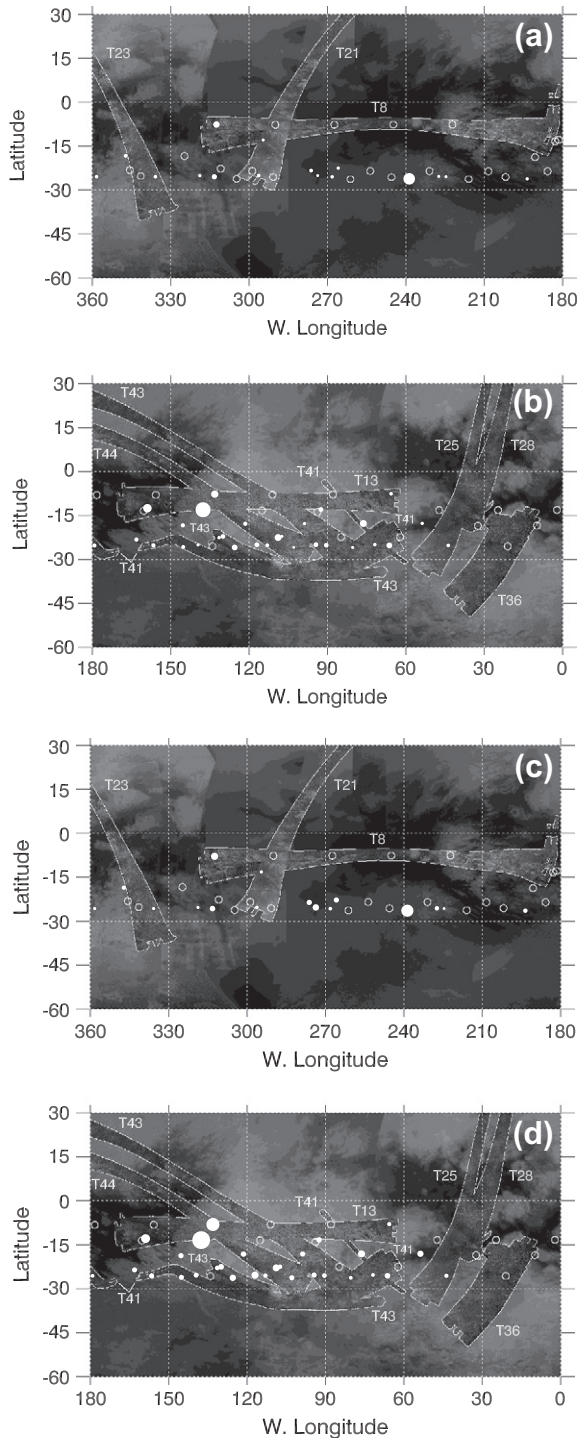


Fig. 17. Cassini SAR tracks from the main mission (through T44) are shown together with the locations of the sub-radar points of the Arecibo/GBT data. In panels (a) and (b) the filled circles indicate the RMS slopes (α) from the scattering function fits with the size of the symbol indicating the value, increasing from 0.2° to 15° . In panels (c) and (d) the filled circles indicate the dielectric constant (ϵ) from the scattering function fits with the size of the symbol indicating the value, increasing from 1.4 to 4.6. The open circles indicate there was no significant specular component in that fit. Panels (a) and (c) are the trailing hemisphere and panels (b) and (d) are the leading hemisphere. The background image is a montage of Cassini ISS images (PIA08399, NASA/JPL/Space Science Institute). The points which directly overlap the Cassini SAR swaths are shown in more detail in Fig. 18.

Ontario Lacus near the southern pole (Wye et al., 2009), this same interpretation of the specular echoes from near-equatorial regions

seems unlikely as no lake features have been observed in Cassini RADAR imagery of these areas and instead extensive dune fields are often seen (Lorenz et al., 2006). In addition, specular reflection of sunlight from a liquid surface has been seen from a high northern latitude area (Stephan et al., 2010), however a wider search including lower latitudes have not detected any such glints (Porco et al., 2005). A smooth surface saturated by liquid hydrocarbons but with no standing liquid may be a possible explanation for this discrepancy. An alternative possibility is that at least some of the specular echoes here arise from reflections from dune fields since these seem to be ubiquitous in the equatorial region of Titan and may also occur in Xanadu. The dunes in these fields have characteristic heights and spacings of order 100 m, but are likely quite smooth on meter scales. However, surfaces that are not azimuthally symmetric or contain periodic structures such as dune fields complicate any interpretation of a radar echo as the properties of the specular component will depend on the viewing geometry in relation to the orientation and mean slope of the dunes. Thus any specular reflection from the dunes may require a fortuitous geometry.

Some Cassini SAR data has been taken across the right latitudes to afford an opportunity to directly correlate the properties of these radar data with specific terrain types over substantial areas of existing Cassini SAR imagery. The relevant SAR swaths from the Cassini main mission are shown in Fig. 17. Two swaths, T8 and T13, were made over nearly equatorial southern latitudes fortuitously matched to the latitude of the sub-Earth location in 2008, and so we matched our observations to cover the same longitude regions. In 2007 one date had also hit the edge of T8 at its western end at about 290°W , 15°S , and two other dates were centered on nearly the same sub-radar location in the western end of T13 at about 160°W , 13.5°S . The T13 strip spans the longitude range $63\text{--}170^\circ\text{W}$ and crosses Xanadu Regio. Three later swaths, T41, T43, and T44, also cross Xanadu and several of our sub-radar locations. The T8 strip covers the longitude range $183\text{--}317^\circ\text{W}$ and includes large areas of dune fields and, near its eastern end, the Huygens landing site at 192.4°W , 10.2°S (Lunine et al., 2008) and the surrounding dark areas that are not dune fields and appear to have been formed or at least modified by fluvial processes. Track T21 also overlaps a portion of T8 and two of our sub-radar locations. Four more Cassini tracks, T23, T25, T28, and T36 span more latitudes but fortuitously crossed a few of our sub-radar points located on the Saturn-facing hemisphere.

Fig. 18 shows the locations of the sub-Earth tracks on segments extracted from the Cassini imagery strips. Several of the Arecibo/GBT spectra from these tracks show small or broad specular echoes, but none show any strong or narrow ones (see Fig. 2 and Table 4). This is somewhat surprising as these locations sample several different terrain types, and there is no obvious strong correlation between the terrain type and the type or presence of specular echo. Several of the locations observed in the T8 swath seem to be dominated by sand dunes (Lorenz and Radebaugh, 2009) but exhibit virtually no specular component at all, indicating that either the surface is rough at 13 cm scales or the porosity is so high that any surface echo is too weak to be detected. The only small specular components seen in the T8 tracks appear in the two westernmost spectra obtained on 2008 February 12 and 13, both of which contain some brighter rugged terrain and less dune fields. The measured specular reflectivities for those two locations were 0.044 and 0.017 (see Table 4) corresponding to dielectric constants of ~ 2.3 and ~ 1.7 , respectively, on the assumption of a homogeneous surface.

No narrow specular echoes were observed for the tracks in Xanadu from SAR swath T13, and there are no terrains within that SAR swath that appear likely to produce narrow specular scattering. This is also surprising in that Arecibo echo spectra obtained

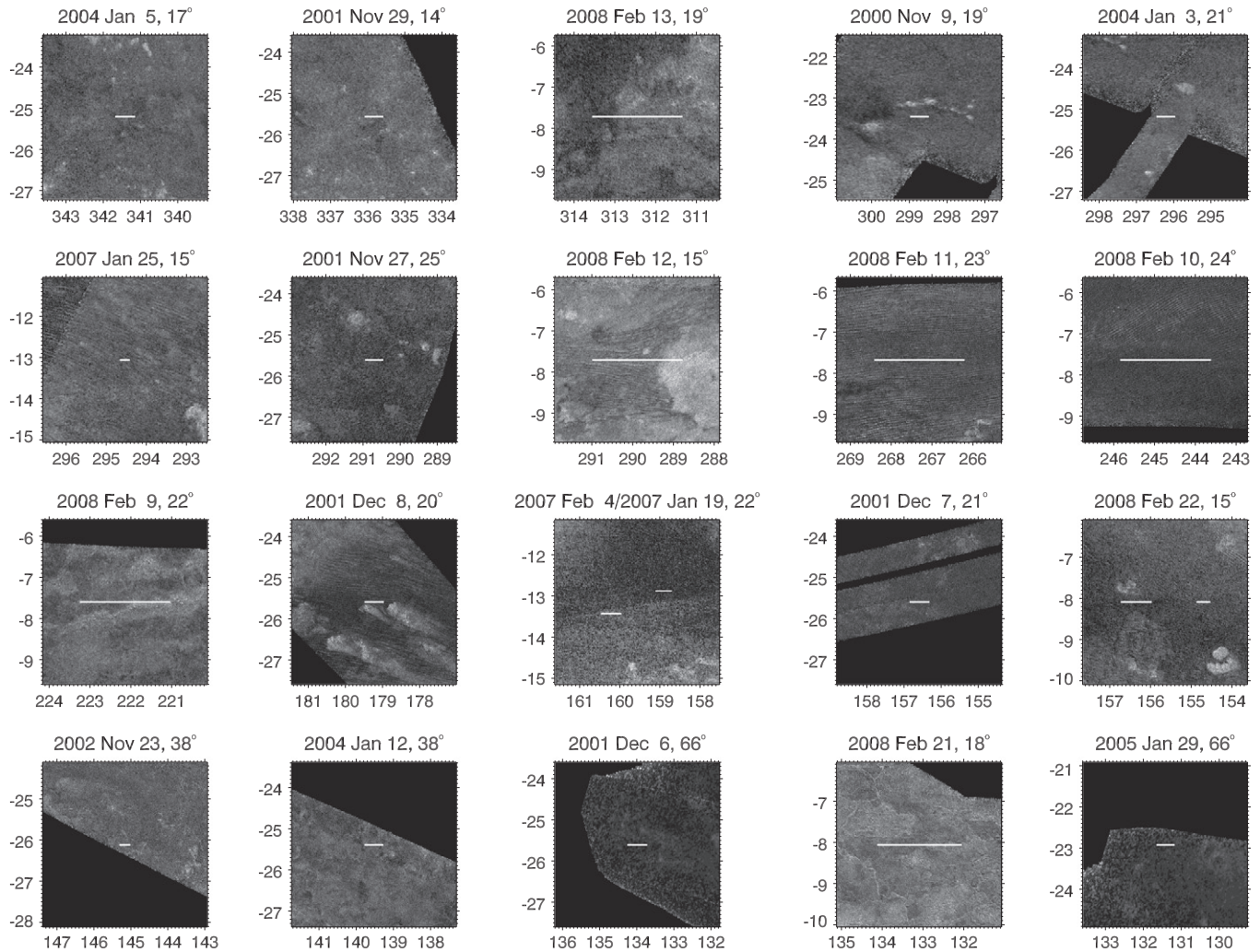


Fig. 18. Locations of the sub-radar tracks in 2008 that overlap the Cassini SAR passes are plotted over cutouts of those radar swaths. The panels have been ordered by their sub-radar longitude moving west to east. Each panel spans 180×135 km around the ground-based radar track, and the resolution of the SAR data here is typically ~ 350 m and their incidence angles at these locations are indicated in the title of each panel.

in prior years at lower latitudes over Xanadu almost always exhibited specular echoes. This implies either a strong latitudinal dependency of the scattering properties of Xanadu or temporal changes over the past several years. Fig. 19 shows coarse histograms of the percentage of significant (three standard deviations) narrow specular ($\alpha < 3^\circ$) echoes seen in the full dataset as a function of latitude and year. Although this includes non-Xanadu locations, there appears to be a real decrease in the type of terrain exhibiting specular echoes as these data track from $\sim 26^\circ\text{S}$ to $\sim 8^\circ\text{S}$ or a change in the surface properties over time since 2004. The latter scenario may be consistent with the rapid evaporation of shallow liquid bodies with scales of tens of kilometers or less over timescales of only a few years (Mitri et al., 2007).

4. Discussion

We have conducted radar observations of Titan using the Arecibo Observatory's 12.6 cm wavelength system. The observations were made during multiple oppositions of the Saturn system and sample sub-radar locations on Titan at near-equatorial southern latitudes and numerous longitudes. The reflectivity variations with longitude mirror those seen at infrared wavelengths and by the Cassini RADAR, with the Xanadu region being more reflective

than average and the trailing hemisphere less reflective. The radar properties of Titan at this wavelength are intermediate between the highly efficient scattering from clean ice surfaces and the low reflectivity of more absorptive surfaces, and it has a polarization ratio indicative of a mix of depolarizing multiple scattering (surface or volume perhaps) and specular-like single surface reflections. We have fit a standard planetary radar scattering law to the radar echo spectrum in order to extract parameters that possibly describe the surface slopes and dielectric constants.

An intriguing feature of these 12.6 cm wavelength radar data is the presence of a narrow specular component whose strength varies dramatically depending on the location of the sub-radar point, at times being very strong while at other times non-existent. The narrowness of this component suggests extremely flat surfaces as would naturally be expected from bodies of standing liquid. However, the sub-radar locations of these features are at near equatorial latitudes, whereas the Cassini RADAR sees these regions dominated by dune fields and other non-liquid features, with lakes seen only at higher latitudes that were not probed here. This discrepancy represents an unresolved puzzle and seems to require invoking an unusual scattering mechanism whereby the surface appears flat on the 12.6 cm wavelength scale but not at the Cassini RADAR 2.2 cm wavelength nor in a way evident at the Cassini SAR resolution.

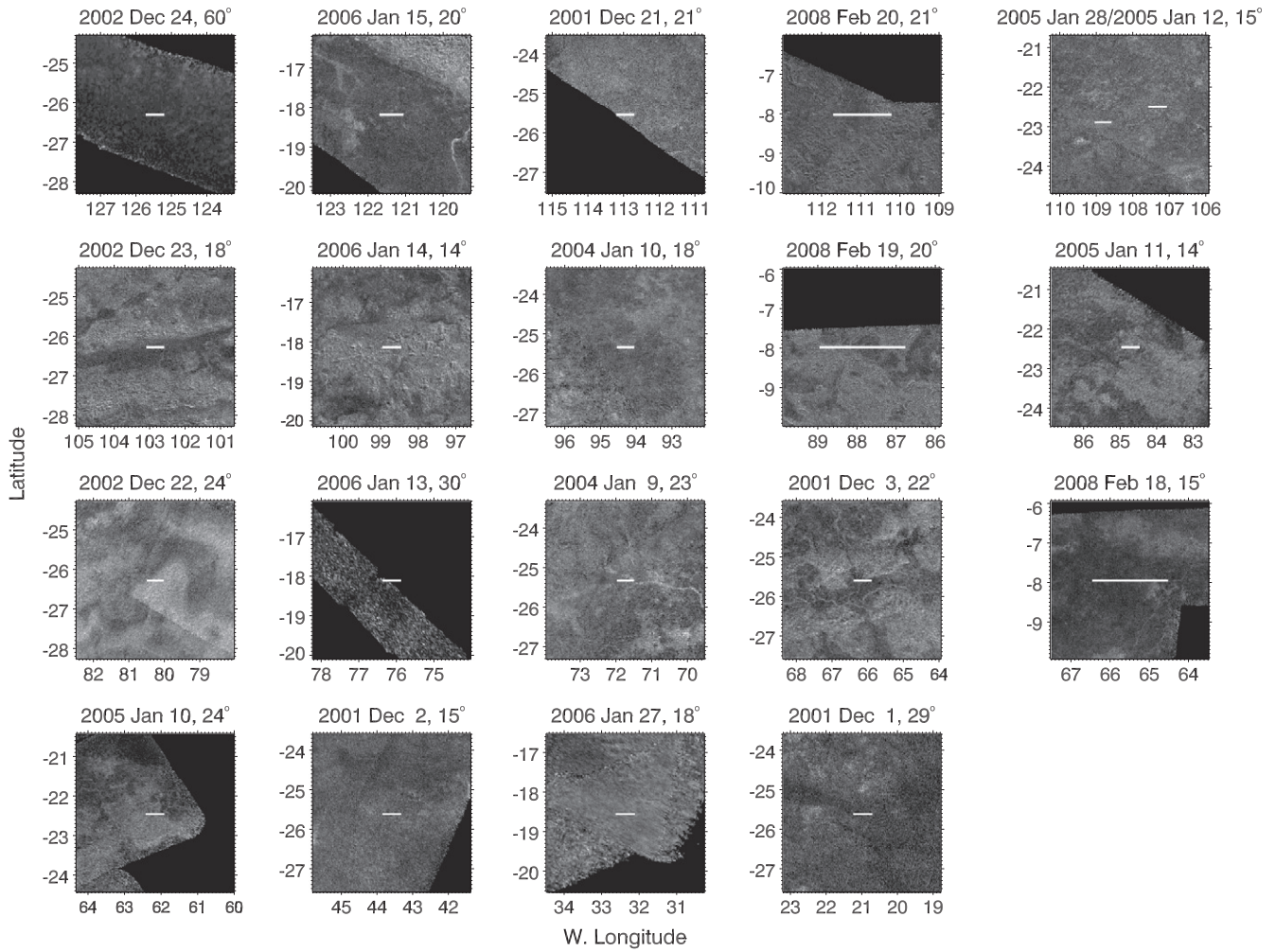


Fig. 18 (continued)

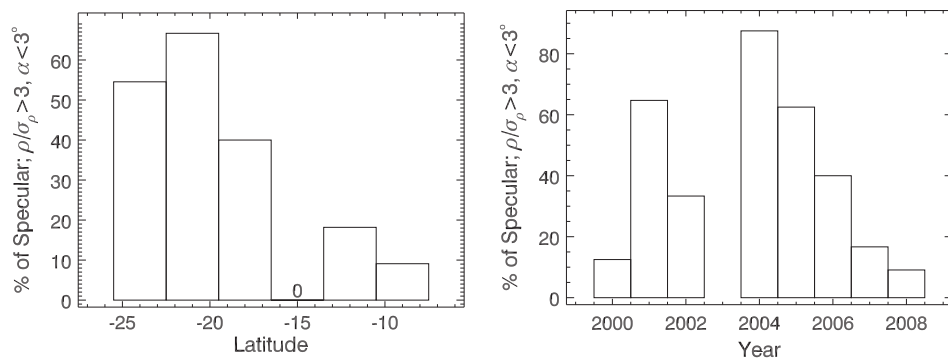


Fig. 19. Percentage of spectra exhibiting a statistically significant specular component, where the scattering model amplitude (ρ) is greater than three deviations, binned by latitude in panel (a) and by observation year in panel (b). There appears to be a real decrease in the number of such components over the observing period as a function of surface location or time.

Acknowledgments

We acknowledge support from the NASA Planetary Astronomy Program (for GJB) and the NASA Planetary Geology and Geophysics Program (for DBC). The Arecibo Observatory is part of the National Astronomy and Ionosphere Center, which is operated by Cornell University under a cooperative agreement with the National Science Foundation. The Green Bank Telescope is operated by the National

Radio Astronomy Observatory, a facility of the National Science Foundation operated under cooperative agreement by Associated Universities, Inc. Ephemerides essential for this work were provided by John Chandler at the Smithsonian Institution and Jon Giorgini at JPL. The staff at the Arecibo Observatory and Green Bank Telescope contributed significantly to the success of the observations. We appreciate the thorough reviews by Lauren Wye and an anonymous reviewer that greatly improved the manuscript.

References

- Atreya, S.K., Adams, E.Y., Niemann, H.B., Demick-Montelara, J.E., Owen, T.C., Fulchignoni, M., Ferri, F., Wilson, E.H., 2006. Titan's methane cycle. *Planet. Space Sci.* 54, 1177–1187.
- Barnes, J.W., Brown, R.H., Soderblom, L., Buratti, B.J., Sotin, C., Rodriguez, S., Le Mouél, S., Baines, K.H., Clark, R., Nicholson, P., 2007a. Global-scale surface spectral variations on Titan seen from Cassini/VIMS. *Icarus* 186, 242–258.
- Barnes, J.W. et al., 2007b. Near-infrared spectral mapping of Titan's mountains and channels. *J. Geophys. Res.* 112, E11006.
- Black, G.J., Campbell, D.B., Carter, L.M., 2007. Arecibo radar observations of Rhea, Dione, Tethys, and Enceladus. *Icarus* 192, 702–711.
- Brown, M.E., Bouchez, A.H., Griffith, C.A., 2002. Direct detection of variable tropospheric clouds near Titan's south pole. *Nature* 420, 795–797.
- Buratti, B.J. et al., 2006. Titan: Preliminary results on surface properties and photometry from VIMS observations of the early flybys. *Planet. Space Sci.* 54, 1498–1509.
- Burr, D.M., Jacobsen, R.E., Roth, D.L., Phillips, C.B., Mitchell, K.L., Viola, D., 2009. Fluvial network analysis on Titan: Evidence for subsurface structures and west-to-east wind flow, southwestern Xanadu. *Geophys. Res. Lett.* 36, L22203.
- Campbell, B.A., 2007. A rough-surface scattering function for Titan radar studies. *Geophys. Res. Lett.* 34, L14203.
- Campbell, D.B., Chandler, J.F., Pettengill, G.H., Shapiro, I.I., 1977. Galilean satellites of Jupiter: 12. 6-Centimeter radar observations. *Science* 196, 650–653.
- Campbell, D.B., Chandler, J.F., Ostro, S.J., Pettengill, G.H., Shapiro, I.I., 1978. Galilean satellites – 1976 radar results. *Icarus* 34, 254–267.
- Campbell, D.B., Black, G.J., Carter, L.M., Ostro, S.J., 2003. Radar evidence for liquid surfaces on Titan. *Science* 302, 431–434.
- Combes, M., Vapillon, L., Gendron, E., Coustenis, A., Lai, O., Wittemberg, R., Sirdey, R., 1997. Spatially resolved images of Titan by means of adaptive optics. *Icarus* 129, 482–497.
- Cordier, D., Mousis, O., Lunine, J.I., Lavvas, P., Vuitton, V., 2009. An estimate of the chemical composition of Titan's lakes. *Astrophys. J. Lett.* 707, L128–L131.
- Downs, G.S., Goldstein, R.M., Green, R.R., Morris, G.A., Reichley, P.E., 1973. Martian topography and surface properties as seen by radar: The 1971 opposition (A2.5). *Icarus* 18, 8–21.
- Elachi, C. et al., 2005. Cassini RADAR views the surface of Titan. *Science* 308, 970–974.
- Elachi, C. et al., 2006. Titan Radar Mapper observations from Cassini's T₃ fly-by. *Nature* 441, 709–713.
- Grasset, O., Sotin, C., Deschamps, F., 2000. On the internal structure and dynamics of Titan. *Planet. Space Sci.* 48, 617–636.
- Griffith, C.A., Owen, T., Miller, G.A., Geballe, T., 1998. Transient clouds in Titan's lower atmosphere. *Nature* 395, 575–578.
- Hagfors, T., 1964. Backscattering from an undulating surface with applications to radar returns from the Moon. *J. Geophys. Res.* 69, 3779–3784.
- Hagfors, T., 1970. Remote probing of the Moon by infrared and microwave emission and by radar. *Radio Sci.* 5, 189–227.
- Harmon, J.K., Campbell, D.B., Ostro, S.J., 1982. Dual-polarization radar observations of Mars – Tharsis and environs. *Icarus* 52, 171–187.
- Harmon, J.K., Slade, M.A., Hudson, R.S., 1992. Mars radar scattering – Arecibo/Goldstone results at 12.6- and 3.5-cm wavelengths. *Icarus* 98, 240–253.
- Heiles, C. et al., 2000. Main Beam and First Sidelobe Parameters for Arecibo's Receiver Systems. Technical Report Arecibo Technical and Operations Memo 2000-4, NAIC, Arecibo, PR.
- Lopes, R.M.C., 2007. Cryovolcanic features on Titan's surface as revealed by the Cassini Titan Radar Mapper. *Icarus* 186, 395–412.
- Lorenz, R.D., 2008. Fluvial channels on Titan: Initial Cassini RADAR observations. *Planet. Space Sci.* 56, 1132–1144.
- Lorenz, R.D., Radebaugh, J., 2009. Global pattern of Titan's dunes: Radar survey from the Cassini prime mission. *Geophys. Res. Lett.* 36, L03202.
- Lorenz, R.D. et al., 2006. The sand seas of Titan: Cassini RADAR observations of longitudinal dunes. *Science* 312, 724–727.
- Lorenz, R.D. et al., 2007. Titan's young surface: Initial impact crater survey by Cassini RADAR and model comparison. *Geophys. Res. Lett.* 34, L07204.
- Lunine, J.I., Stevenson, D.J., Yung, Y.L., 1983. Ethane ocean on Titan. *Science* 222, 1229–1230.
- Lunine, J.I. et al., 2008. Titan's diverse landscapes as evidenced by Cassini RADAR's third and fourth looks at Titan. *Icarus* 195, 415–433.
- Mitri, G., Showman, A.P., Lunine, J.I., Lorenz, R.D., 2007. Hydrocarbon lakes on Titan. *Icarus* 186, 385–394.
- Muhleman, D.O., Grossman, A.W., Butler, B.J., Slade, M.A., 1990. Radar reflectivity of Titan. *Science* 248, 975–980.
- Muhleman, D.O., Grossman, A.W., Slade, M.A., Butler, B.J., 1993. Titan's radar reflectivity and rotation. *Bull. Am. Astron. Soc.* 25, 1099.
- Muhleman, D.O., Grossman, A.W., Butler, B.J., 1995. Radar investigations of Mars, Mercury, and Titan. *Annu. Rev. Earth Planet. Sci.* 23, 337–374.
- Ostro, S.J., 1993. Planetary radar astronomy. *Rev. Mod. Phys.* 65, 1235–1280.
- Ostro, S.J., Campbell, D.B., Simpson, R.A., Hudson, R.S., Chandler, J.F., Rosema, K.D., Shapiro, I.I., Standish, E.M., Winkler, R., Yeomans, D.K., 1992. Europa, Ganymede, and Callisto – New radar results from Arecibo and Goldstone. *J. Geophys. Res.* 97, 18227–18244.
- Ostro, S.J. et al., 2006. Cassini RADAR observations of Enceladus, Tethys, Dione, Rhea, Iapetus, Hyperion, and Phoebe. *Icarus* 183, 479–490.
- Owen, T., 1982. The composition and origin of Titan's atmosphere. *Planet. Space Sci.* 30, 833–838.
- Paillou, P., Mitchell, K., Wall, S., Ruffié, G., Wood, C., Lorenz, R., Stofan, E., Lunine, J., Lopes, R., Encrenaz, P., 2008. Microwave dielectric constant of liquid hydrocarbons: Application to the depth estimation of Titan's lakes. *Geophys. Res. Lett.* 35, L05202.
- Porco, C.C. et al., 2005. Imaging of Titan from the Cassini spacecraft. *Nature* 434, 159–168.
- Radebaugh, J. et al., 2008. Dunes on Titan observed by Cassini RADAR. *Icarus* 194, 690–703.
- Sagan, C., Dermott, S.F., 1982. The tide in the seas of Titan. *Nature* 300, 731–733.
- Sears, W.D., 1995. Tidal dissipation in oceans on Titan. *Icarus* 113, 39–56.
- Seidelmann, P.K. et al., 2006. Report of the IAU/IAG working group on cartographic coordinates and rotational elements: 2006. *Celest. Mech. Dynam. Astron.* 98 (3), 155–180.
- Simpson, R.A., Harmon, J.K., Zisk, S.H., Thompson, T.W., Muhleman, D.O., 1992. Radar determination of Mars surface properties. In: Kieffer, H.H., Jakosky, B.M., Snyder, C.W., Matthews, M.S. (Eds.), *Mars*. Univ. of Arizona Press, Tucson, pp. 652–685.
- Smith, P.H., Lemmon, M.T., Lorenz, R.D., Sromovsky, L.A., Caldwell, J.J., Allison, M.D., 1996. Titan's surface, revealed by HST imaging. *Icarus* 119, 336–349.
- Stephan, K., 2010. Detection of a specular reflection on Titan by Cassini-VIMS. *Lunar Planet. Sci.* 41, 1692–1693.
- Stofan, E.R. et al., 2007. The lakes of Titan. *Nature* 445, 61–64.
- Sultan-Salem, A.K., Tyler, G.L., 2006. Generalized fractal-based laws for scattering from planetary surfaces: A unifying scale-explicit paradigm. *J. Geophys. Res.* 111, E06S08.
- Sultan-Salem, A.K., Tyler, G.L., 2007. Revisiting Titan's Earth-based scattering data at 13 cm-λ. *Geophys. Res. Lett.* 34, L12201.
- Thompson, W.R., Squyres, S.W., 1990. Titan and other icy satellites: Dielectric properties of constituent materials and implications for radar sounding. *Icarus* 86, 336–354.
- Turtle, E.P., Perry, J.E., McEwen, A.S., DelGenio, A.D., Barbara, J., West, R.A., Dawson, D.D., Porco, C.C., 2009. Cassini imaging of Titan's high-latitude lakes, clouds, and south-polar surface changes. *Geophys. Res. Lett.* 36, L02204.
- Wall, S.D. et al., 2009. Cassini RADAR images at Hotei Arcus and western Xanadu, Titan: Evidence for geologically recent cryovolcanic activity. *Geophys. Res. Lett.* 36, L04203.
- Warren, S.G., 1984. Optical constants of ice from the ultraviolet to the microwave. *Appl. Opt.* 23, 1206–1225.
- Wye, L.C., Zebker, H.A., Ostro, S.J., West, R.D., Gim, Y., Lorenz, R.D., The Cassini RADAR Team, 2007. Electrical properties of Titan's surface from Cassini RADAR scatterometer measurements. *Icarus* 188, 367–385.
- Wye, L.C., Zebker, H.A., Lorenz, R.D., 2009. Smoothness of Titan's Ontario Lacus: Constraints from Cassini RADAR specular reflection data. *Geophys. Res. Lett.* 36, 16201–+.
- Zebker, H.A., Wye, L.C., Janssen, M.A., Cassini RADAR Team, 2008. Titan's surface from reconciled Cassini microwave reflectivity and emissivity observations. *Icarus* 194, 704–710.